*Revised Manuscript with No changes marked
Click here to download Revised Manuscript with No changes marked: Landi et al. LITHOS revised.docx

Deciphering textural and chemical zoning of K-feldspar megacrysts from Mt. Amiata Volcano (Southern Tuscany, Italy): insights into the petrogenesis and abnormal crystal growth

Patrizia Landi (1, 2), Sonia La Felice (2), Maurizio Petrelli (3, 4), Luigina M. Vezzoli (2, 5), Claudia Principe (2)

(1) Istituto Nazionale di Geofisica e Vulcanologia, sezione di Pisa, Italy
(2) Istituto di Geoscienze e Georisorse, Consiglio Nazionale delle Ricerche, Pisa, Italy
(3) Dipartimento di Fisica e Geologia, Università degli Studi di Perugia, Italy
(4) Istituto Nazionale di Fisica Nucleare (INFN), Sezione di Perugia, Italy
(5) Dipartimento di Scienza e Alta Tecnologia, Como, Università degli Studi dell'Insubria, Italy

Corresponding author: Sonia La Felice, e-mail: sonia.lafelice@igg.cnr.it

Abstract

This study reports the complex textural and chemical features of K-feldspar megacrysts (up to 5 cm long) hosted in trachydacitic lava flows, lava domes, and *coulées* from Mt. Amiata volcano (Tuscan Magmatic Province, Central Italy). Backscattering and cathodoluminescence imaging, coupled with core to rim major and trace elements patterns, reveal complex zoning, and resorption surfaces associated with sharp chemical variations (e.g., Sr and Ba). These zoning patterns originated by disequilibrium and re-equilibration events, related to the repeated influx of mafic magmas or convective motions in the trachydacitic magma reservoir. Multiple mafic magma refilling occurences are also supported by the field record of abundant microgranular magmatic enclaves in the studied products. Our results highlight that the abnormal dimension of the studied K-feldspars originates by the interplay between petrological and kinetic processes involving: (i)

extensive dissolution; (ii) heterogeneous nucleation; (iii) alternation of spasmodic growth events in disequilibrium and near-equilibrium crystallization. The repeated influx of hotter magmas and reheating can determine the thermal condition to the growth of few, large K-feldspar megacrysts. Also, the strong textural and chemical similarities observed in the K-feldspar megacrysts from Mt. Amiata volcanic rocks and Mt. Capanne monzogranite (Elba Island, Central Italy) support the hypothesis of a phenocrystic origin of intrusive K-feldspar megacrysts.

Keywords

K-feldspar megacrysts; feldspar microtexture; chemical zoning; trace elements; magma mixing; dissolution/recrystallization; Mount Amiata, Italy.

1. Introduction

The origin of K-feldspar megacrysts in igneous rocks (both plutonic and volcanic) is a fascinating and still debated petrologic argument. K-feldspar megacrysts, up to 15-20 cm long, are quite common in plutonic rocks (Cox et al., 1996; Gagnevin et al., 2004, 2005; Moore and Sisson, 2008; Paterson and Vernon, 2002; Słaby et al., 2007, 2017; Vernon, 1986) and one of the leading open questions about their origin refers to the timing of their growing (i.e. the so called "late" or "early" formation hypothesis). The late formation hypothesis implies a porphyroblastic growth under subsolidus conditions, by textural coarsening promoted by thermal cycling, possibly associated with fluid migration (Glazner and Johnson, 2013; Johnson and Glazner, 2010). On the contrary, the early formation hypothesis favours a magmatic origin suggesting that K-feldspar megacrysts develop as phenocrysts from the melt phase of magma. Vernon (1986) presented and discussed many points of evidence in support of a magmatic origin and, more recently, many additional textural and chemical studies of the megacrysts from different plutons support this interpretation (Cox et al., 1996; Higgins, 1999; Moore and Sisson, 2008; Słaby et al., 2007, 2017;

53 Vernon, 2010; Vernon and Paterson, 2008). Oscillatory zoning of many K-feldspar megacrysts has
54 been considered as evidence of their magmatic origin by Vernon (1986). In addition, oscillatory
55 zoning and resorption surfaces related to chemical and textural discontinuities, have been
56 commonly linked to the intrusion of hotter magmas into a silicic magma reservoir and/or convection
57 (Cox et al., 1996; Gagnevin et al., 2008; Moore and Sisson, 2008; Słaby et al., 2007, 2017). These
58 authors consider the presence of mafic to felsic enclaves in some megacrystic granitic rocks an
59 additional evidence of magma mixing. Assuming a phenocrystic origin, several hypotheses have
60 been advanced as to why feldspar crystals reach very large dimensions. According to Vernon
61 (1986) the large size of the K-feldspar is strictly connected with the crystal kinetics (nucleation and
62 growth rate), in particular, the nucleation difficulty of the K-feldspar in granitic melts (see also
63 Vernon, 2004, pp 46-54; Vernon, 2010). Higgins (1999) suggests that K-feldspar megacrysts are
64 formed by textural coarsening which is promoted by temperature cycling, during which the magma
65 temperature is buffered close to the liquidus temperature of the K-feldspar for a long time.
66 According to Moore and Sisson (2008), repeated reheating of the granitic pluton in the Sierra
67 Nevada Batholith, due to surges of new, hotter melt, provides the ideal environment for the growth
68 of the extraordinarily large K-feldspars.

69 Although less common, K-feldspar megacrysts (i.e., sanidine megacrysts) are also found in
70 volcanic rocks. Examples are the trachytic to rhyolitic lavas and lava domes from Mt. Amiata and
71 Roccastrada (Tuscany, Central Italy; Balducci and Leoni, 1981) and other volcanic occurrences in
72 different magmatic setting (e.g., Perini et al., 2003; Higgins, 2011; Moussallam et al., 2015). In
73 these case studies, there are no doubts about the magmatic origin of the megacrysts. However, as
74 for the megacrysts in plutonic environment, the mechanisms and the dynamics governing their
75 formation and growth are still widely debated deserving further investigations. As an example,
76 Balducci and Leoni (1981) suggested that the unusual dimensions of sanidine megacrysts are linked
77 to the high growth rate of K-feldspars in trachytic and rhyolitic melts. Higgins (2011), following the
78 same model applied in plutonic context (Higgins, 1999), proposed that megacrysts in dacites from

79 the Taapaca volcano are the result of textural coarsening cycles that were enabled by repeated
80 variations of the magma temperature (around the liquidus temperature of the sanidine) in response
81 to injections of more mafic magmas. Finally, Moussallam et al. (2015) suggested that the
82 anorthoclase megacrysts from Erebus volcano (Antartica) originated by complex dynamics
83 occurring in a vigorously convecting reservoir, and bi-directional magma transport between the
84 reservoir and the overlying lava lake via the conduit.

85 The primary aim of this study is to shed new light on the processes and the dynamics
86 governing the origin and crystallization of K-feldspar megacrysts in igneous rocks by focusing on
87 the textural characteristics and compositional zoning of K-feldspar megacrysts hosted in
88 trachydacitic effusive products from Mt. Amiata Volcano (Tuscany, Central Italy). We used in-situ
89 major and trace element analyses on crystals and glasses combined with high-resolution electron
90 back-scattered and cathodoluminescence imaging. In particular, we focus on compatible trace
91 elements in K-feldspars (i.e., Sr and Ba). The slow diffusivities of these elements, in both alkali
92 feldspar and plagioclase, preserve the primary chemical heterogeneity under variable thermal
93 conditions for extended periods (Cherniak, 2002; Singer et al., 1995), making chemical zoning of
94 the feldspar one of the more robust geochemical indicators of magma evolution (e.g., Cox et al.,
95 1996; D'Oriano et al., 2017; Gagnevin et al., 2004, 2005; Ginibre et al., 2004; Słaby et al., 2007,
96 2008). Moreover, the study of the K-feldspar megacrysts is largely facilitated in effusive rocks
97 because volcanic crystals keep the original zoning almost unaltered. Otherwise, despite the plutonic
98 K-feldspar megacrysts preserve magmatic shape and microstructures (e.g. oscillatory zoning)
99 (Vernon, 2004; Vernon and Paterson, 2008; Vernon, 2010), they typically show evidence of
100 subsolidus exsolution, which make accurate chemical analysis difficult to obtain (Vernon, 1986).
101
102 **2. Geological background**
103

Mt. Amiata, sited in southern Tuscany, is the youngest volcano (about 300-230 ka; Laurenzi et al., 2015) of the Tuscan Magmatic Province (TMP), which comprises several mafic to silicic intrusive and effusive centres spread out in southern Tuscany and Tuscan archipelago. They include high-potassium calc-alkaline (HKCA), shoshonitic (SHO), potassic alkaline (KS) and ultrapotassic lamproitic rocks (Peccerillo et al., 2017 and references therein).

According to geochemical and isotopic constraints (e.g. Cadoux and Pinti, 2009; Conticelli et al., 2015; Cristiani and Mazzuoli, 2003; Giraud et al., 1986; Peccerillo et al., 1987; Poli et al., 1984; Rombai et al., 1995; Van Bergen et al., 1983), Mt. Amiata experienced a complex compositional evolution, also involving magma mixing processes, between an ultra-potassic mafic magma (with geochemical characteristics typical of the Roman Magmatic Province, RMP) and a calc-alkaline silicic magmatic system probably crustal-derived (with geochemical characteristics typical of the TMP). The roof of the shallow reservoir has been estimated at depth of 5-7 Km (Gianelli et al., 1988).

The volcanic activity of Mt. Amiata mainly developed along an ENE-WSW-trending structural alignment, and it is dominated by the emplacement of lava flows, lava domes, and *coulées*. The most recent geological interpretation suggests two main periods of activity corresponding to an older Bágnore Synthem and a younger Mt. Amiata Synthem, separated by a major unconformity (Principe et al., 2017, 2018; Vezzoli and Principe, 2017). The Bágnore Synthem comprises two Subsynthems (Fig. 1) and is characterized by the emission of several lava flows (up to 8 km long) and the emplacement of only one exogenous lava dome with *coulées*, included inside Montearioso Subsynthem. The Mt. Amiata Synthem comprises three Subsynthems, among which the oldest Valle Gelata Subsynthem (Fig. 1) is characterized by both extensive lava flows that reach 4-6 km in length and exogenous lava domes; while the younger two Subsynthems (named Madonna degli Scout and Prato della Contessa; Fig. 1) include several exogenous lava domes with *coulées* and small lava flows.

129 The composition of the erupted products ranges from latite to trachydacite (SiO_2 = 57-68 wt
130 % and Na_2O+K_2O = 7-9 wt %; Fig. 2) (Cadoux and Pinti, 2009; Conticelli et al., 2015; Ferrari et al.,
131 1996; La Felice et al., 2017; Poli et al., 1984; Rombai et al., 1995). Also, they contain, in variable
132 proportion, millimetric to pluri-decimetric size metasedimentary xenoliths and microgranular
133 magmatic enclaves. The latter are characterized by compositions ranging from trachybasalt to latite
134 (SiO_2 = 47-59 wt % and Na_2O+K_2O = 5-8 wt %; Fig. 2) (Rombai et al., 1995; Van Bergen et al.,
135 1983). In general, Mt. Amiata lava flows are highly porphyritic, medium to coarse grained, with a
136 glassy groundmass commonly showing perlitic fractures, and, sometimes, spherulitic textures. The
137 most abundant phenocrysts are plagioclase and K-feldspar (mainly fragments of broken crystals),
138 orthopyroxene and biotite, ±clinopyroxene. Embayed quartz, and other accessory minerals (i.e.,
139 apatite, ilmenite, and zircon) are rare. All the lava domes, *coulées,* and the few short lava flows of
140 the younger Mt. Amiata Synthem have similar mineral paragenesis, but are characterized by the
141 distinctive presence of K-feldspar megacrysts (from 1 to 5-6 cm long) coupled with abundant
142 microgranular, magmatic enclaves (Cadoux and Pinti, 2009; Conticelli et al., 2015; Ferrari et al.,
143 1996; La Felice et al., 2017).
144
145 **3. Methods**
146
147 *3.1 Sampling*
148
149 The investigated K-feldspar megacrysts were collected from three samples (AMT60,
150 AMT95, AMT110) belonging to the three Subsynthems of the younger Mt. Amiata Synthem (see
151 Fig. 1 for location map). In particular, AMT60 was collected from the Coderino lava flow
152 (Coderino formation, Valle Gelata Subsynthem; Principe et al., 2017), AMT 95 comes from the top
153 of the Mt. Amiata exogenous lava dome (La Vetta formation, Madonna degli Scout Subsynthem;
154 Principe et al., 2017), and AMT110 was sampled from a lava *coulées* of the La Montagnola

exogenous lava dome (La Montagnola formation, Prato della Contessa Subsynthem; Principe et al., 2017). Some crystals were collected in the field, extracting them from more friable vesicular lava samples; others were manually separated from the host rock in the laboratory. Unbroken megacrysts, or partially fractured crystals in which the original shape was easily reconstructed, were selected. They were cut through the approximate geometric centre in order to expose all the growing layers including the innermost core. Twenty megacrysts were processed for chemical and textural analyses. Among them five megacrysts were selected for trace element analysis.

3.2 Petrography and textural study

The modal abundance (volume fraction) of K-feldspar megacrysts larger than 1 cm were carried out on samples-hand specimens. The samples were cut into slabs 10–20 cm in length (total surface ~ 0.1 m^2 for each sample) and scanned using a planar scanner (600 dpi). The margins of K-feldspar megacrysts larger than 1 cm were outlined in a vector-drafting program (Adobe Illustrator). Crystal outlines were then filled and exported as TIFF files, and the obtained greyscale images were processed using the ImageJ software (Schindelin et al., 2012). The modal content of <1 cm crystals was determined on thin sections using an optical microscope equipped with a point counter. In each sample, ~ 2000 points were counted excluding bubbles.

Textural investigations were performed at the Istituto Nazionale di Geofisica e Vulcanologia (INGV), in Pisa (Italy) using an optical microscope and a Zeiss EVO MA 10 Scanning Electron Microscope (SEM), capturing selected Back Scattered Electron (BSE) and cathodoluminescence (CL) images. The entire image of each K-feldspar megacryst was assembled from a mosaic of 50-120 greyscale images.

3.3 Mineral and glass analyses

Preliminary major element composition of minerals was performed using a Zeiss EVO MA 10 SEM, equipped with an Oxford ISIS micro-analytical EDS system at the INGV, Pisa (Italy). The analytical error, calculated using international standards, is generally lower than 2% for oxides with concentrations >10 wt%, lower than 10% for oxides between 1 and 10 wt%, and better than 30% for concentrations < 1 wt%.

Trace elements composition of selected K-feldspars, plagioclases, and glasses were performed at the Dipartimento di Fisica e Geologia, University of Perugia (Italy) by Laser Ablation-Inductively Coupled Plasma-Mass Spectrometry (LA-ICP-MS). The instrumentation consisted in a Teledyne Photon Machine G2 laser ablation device, equipped with a two-volume HelEx 2 cell, and coupled to a Thermo Fischer Scientific iCAP Q quadrupole mass spectrometer (Petrelli et al., 2016a). A circular 20 μm spot size, a repetition rate of 8Hz, and a laser fluence of ~3.5 Jcm^{-1} have been utilized. Ablation times were about 30 seconds per spot, preceded by a 25 second background measurement and followed by 25 seconds of washout. Data reduction was completed with the Iolite 3 software (Paton et al., 2011). The NIST SRM 610 (Pearce et al., 1997) glass and the USGS BCR2G (Wilson, 1997) reference materials were used as calibrator and quality control, respectively. The SiO_2 concentrations obtained by electron microprobe were used as internal standard. Under the reported analytical conditions, the precision is better than 10% for concentrations above 0.1 ppm and better than 5% above 20 ppm; accuracy is always better than 10% (Petrelli et al., 2016b).

Major elements analyses at the same locations of trace element determinations (i.e., close to LA craters) were performed using a JEOL JXA-8200 electron microprobe (EMP) equipped with a WDS/EDS combined system at the INGV, Rome (Italy). A beam size of 5-μm was used for feldspars and a defocused beam, with a spot size of 10 μm, for glasses (15 kV voltage, 5 nA beam current). The accuracy of WDS analyses was calculated using international standards (SiO_2<1%; Al_2O_3<2%; Na_2O<9%; K_2O<2%; CaO<2%).

4. Results

4.1 Petrochemical data

The studied rocks are trachydacite with SiO_2 ~ 61.5-62.3 wt %, K_2O ~ 5.5-6.0 wt %, and MgO ~ 1.7-2.6 wt % (Table 1, Fig. 2). They have a crystal content of 35-37 vol% (Table 2) mainly composed of plagioclase (11-13 vol%; An 45-86), K-feldspar (11-14 vol%; Or 76-83), orthopyroxene (5 vol%; Mg# 42-58), clinopyroxene (1-5-vol%; Mg# 59-89; Fs 6-24; Wo 39-51), biotite (2-4 vol%), and minor ilmenite. Among the K-feldspars a 3.5-5% by volume are megacrysts with an average length of 2-3 cm and a maximum length of 5-6 cm. They are commonly euhedral although are rarely completely intact, and can present smoothly rounded margins. K-feldspar phenocrysts <1cm are mostly fragments of broken crystals. Megacrysts and phenocrysts have the same major-element chemical composition ~Or 76-83 (Fig. 3). Millimetric to decimetric microgranular magmatic enclaves with amoeboid shape are abundant. They may contain K-feldspar megacrysts inherited from the host silicic rock. Metasedimentary xenoliths of tabular shape and aggregates of minerals (mainly plagioclase, orthopyroxene, and biotite) are also present. Sample AMT60 has a glassy groundmass with perlitic texture that locally is highly vesicular with fibrous glass portions. Sample AMT110 has heterogeneous groundmass showing flow banding with alternating glassy portions with perlitic cracks, and microcrystalline portions characterized by devitrification textures (spherulites) with the precipitation of secondary minerals in vesicles (e.g., cristobalite). Sample AMT 95 shows hypocrystalline groundmass with abundant plagioclase, K-feldspar and clinopyroxene microlites. The glassy groundmass analyzed in AMT60 and AMT110 has a homogenous rhyolitic composition with SiO_2 ~75-76 wt %, Al_2O_3 ~11.7-12.3 wt %, and K_2O ~6.9-7 wt %.

4.2 *K-feldspar megacrysts*

233

234 *Macroscopic shape*

235 The studied K-feldspar megacrysts are simple prismatic crystals and tabular Carlsbad twins.
236 The crystals are mostly characterized by a {010} tabular habit with the maximum elongation
237 parallel to the c-axis (Fig. 4a, c). A precise quantitative information on their size and shape is
238 limited because the crystals are mostly embedded in the groundmass, and the best exposure is found
239 only on weathered surfaces (Fig. 4a, b, c). Megacrysts usually show a dusty internal portion,
240 crowded with mineral, melt inclusions and vesicles surrounded by a clear corona (Fig.4d).

241

242 *Microscopic texture*

243 Backscattered electron and cathodoluminescence images highlight that compositional and
244 textural zoning is ubiquitous in the investigated K-feldspar megacrysts. Zoning is well shown by
245 different grey tones both in BSE and CL images (Fig. 5a1, a2). Although there is no systematic
246 correlation between brightness in CL images and chemical composition of the mineral (Marshall,
247 1988), a comparison between BSE and CL images show that zoning pattern in CL (Fig. 5a2) images
248 reproduce the zoning observed in BSE (Fig. 5a1), which are conversely strictly related to chemical
249 changes. Thus, in this case, changes of the grey tone in CL images is also associated with
250 compositional variations and can be discussed as evidence of chemical zoning. CL images were
251 mostly used for describing the texture of the studied crystals, because they highlight better than
252 BSE images the complicated zoning of the studied feldspar.

253 At the microscopic scale, the dusty internal portion of the crystals exhibits a complex texture
254 due to the occurrence of large patchy zoned cores crowded with minerals grains and large melt
255 inclusions with irregular shape and vesicles (see in particular Fig. 5a, b, c, d). The cores are
256 commonly surrounded by approximately concentric thick layers, each of them passing towards the
257 outer edge, from bright, patchy zoned layers, to Dark Oscillatory zoned Layers (hereafter DOL)
258 (Fig. 5a, b, c). Deep resorption surfaces mainly develop on the DOL and are highlighted by

259 irregular shapes, deep embayments, rounded boundaries or unconformities. Remnants of deeply
260 resorbed DOL are abundant (Fig. 5a2, b, c). Several deep resorption surfaces are recognized in the
261 largest megacrysts, where the dusty internal portion spreads over almost all the crystal volume (Fig.
262 5a, b, c). The smaller megacrysts record fewer dissolution events and usually show a patchy zoned
263 core crowded with inclusions (minerals, glass, and vesicles) (Fig. 5d, e). Concentric alignments of
264 mineral grains are found in many megacrysts and commonly surround highly irregular resorption
265 surfaces associated with dissolution events (Fig. 5b, c, d). They follow the layer boundaries, are
266 euhedral to subhedral and can be distributed with their long axes parallel to the layer boundary.
267 When the megacryst engulfs mineral grains, large pockets filled with glass formed around the
268 inclusion. Zoned plagioclase, up to 1-2 mm long, is the most abundant inclusion mineral, followed
269 by biotite, pyroxene, oxides, apatite, and small (few micrometres) grains of zircon. The dusty
270 internal portion of the crystals is surrounded by a concentric, oscillatory zoned corona, 2-3 mm
271 thick, which has the same textural characteristics of the interior DOL.

272 Within the DOL, a progressive shift from bright to dark zones is observed in each layer,
273 whereas the contact among dark and bright zones is abrupt. The external boundaries of the darker
274 layers are subhedral to anhedral with rounded and/or lobate shape and can cross-cut the previous
275 layers. The thickness of each layer ranges from 250-300 μm to few tens of μm. These surfaces
276 originated by a relatively weak (or less disrupting) dissolution event during which at least 150 μm
277 of the crystal can be resorbed (Fig. 6).

278 K-feldspar aggregates are also found in the analyzed samples. In particular, in sample
279 AMT95 many megacrysts result from clustering and intergrowth of several millimetre-sized
280 crystals. Large crystal aggregates with irregular shape can form the core of the megacrysts. Mutual
281 attachment of several grains is well shown by the zoning patterns inside the megacrysts that mirror
282 different optical orientation between adjacent growing grains (Fig. 5e). After aggregation, the grain
283 clusters develop a common overgrowth.
284

285 *Chemical zoning*

286 Five representative K-feldspar megacrysts were selected for the study of major and trace
287 element variations. The megacrysts are sanidine with composition ranging between Or76 and Or83
288 (An 1-4, Ab 16-21) and large trace elements variability (Ba ~1100-8800 ppm; Sr ~650-2350 ppm;
289 Eu ~2.5-7.3 ppm; Rb ~350-450 ppm). Core to rim compositional transects reveal chemical
290 oscillatory zoning patterns coupling the textural discontinuities observed in BSE and CL images. In
291 detail, Figure 7 displays Ba and Sr variation within the studied crystals. The area rimward of the
292 main resorbed surfaces shows a Ba increase commonly of 1000-2000 ppm, up to 4000 ppm. The
293 transition from low- to high Ba layers is generally sharp, whereas Ba content in layers between two
294 resorbed surfaces usually decreases outward the crystal (Fig 7b). As a whole, Sr content variations
295 reproduce the Ba trend with an increase rimward of the resorbed surfaces from 100-200 ppm up to
296 800 ppm. The patchy zoned areas show irregular oscillations, while the DOLs, both within the dusty
297 area and the outer corona, exhibit more regular trends characterized by saw-tooth zoning with a
298 gradual Ba decrease outwards of each layer (Fig. 6). The Ba content in each layer varies from about
299 100 up to 350 ppm. The rims (<200 μm) have Ba and Sr contents of ~1570-2540 ppm and ~650-
300 890 ppm, respectively.

301 There is not a clear correlation between the mol% Or and the abundance of compatible trace
302 elements. Rb positively correlates with Ba, Sr and Eu (Fig. 8). Two compositional groups are
303 distinguished in the Rb/Sr vs. Ba diagram: i) the main group shows an increase of Rb/Sr ratio from
304 ~0.3 to ~0.6 which is coupled with a Ba decrease from ~5000 to ~1000 ppm; ii) the patchy cores of
305 the crystals AMT60_cr2 and AMT95_cr1 and the patchy layer between 1 and 2 cm from the rim
306 within AMT110_cr2 show higher Ba contents and, as a whole, depict a line of descent in the range
307 Rb/Sr ratio 0.15 - 0.60 and Ba 8800-3800 ppm. This second compositional group is also
308 characterized by a distinct enrichment of Pb and Li (Fig. 8 and Supplementary Table 1). The
309 different enrichment of trace elements is not related to a specific texture. Indeed, all the high-Ba

310 portions within the crystals have patchy texture, but patchy textured zones with relatively low-Ba
311 content are also present.
312
313 *Plagioclase inclusions*
314 Mineral inclusions in the K-feldspar megacrysts show variable dimension from tens of
315 micrometres to 1-2 mm. The dimension of the largest inclusions is comparable with that of the
316 phenocrysts in the groundmass.
317 Plagioclase is the most abundant mineral inclusion. It usually results from the clustering of
318 small grains (Fig 6 and Fig. 9a, b) and shows cores with a wide compositional variation, from An48
319 to An78, rimmed by an An-poor layer (An 45-58) with euhedral outer margins. Sporadic crystals
320 show a direct zoning from An69 to An48 with euhedral growth boundaries (Fig. 9c). Cores host
321 many melt inclusions and bubbles with either irregular or elongated nearly rectangular shaped,
322 aligned parallel to the main axis of the crystal. Embayment enclosed by euhedral edges are also
323 present on the rim. Melt inclusions and bubbles appear to be embedded during the crystal growth or
324 when two grains with irregular boundary attached (Fig. 9a, b). Although these crystal shapes are not
325 the typical skeletal or hopper texture that originates at high crystal growth rate under high
326 undercooling (Fenn, 1977; Lofgren, 1974), the entrapment of large melt pockets and the formation
327 of large embayments enclosed by euhedral edges point to a fairly high growth rate.
328 Complex resorption and growth features characterize the larger crystals (~ 1-2 mm). The
329 cores are characterized by the occurrence of nearly homogeneous, strongly resorbed areas An50-
330 An55 (dark grey in Fig. 9d) and sieve textured, patchy zoned sectors (bright zones in Fig. 9d) with
331 composition ranging between An60 and An80. The An rich zones are intensely altered into hydrous
332 aluminium silicates (allophane). The outer rims have nearly homogeneous composition ~An50.
333 Compatible trace elements in the plagioclase inclusions increase with An increasing. Sr ranges from
334 ~700 ppm in An-poor plagioclase up to ~1100 ppm in the An-rich patchy zones. As Sr, also Eu
335 increases from 2.5 ppm in the An-poor zones to 3.9 ppm in the An-rich zones (Fig. 10).

Both the texture and composition of plagioclase inclusions show characteristics comparable to those of the plagioclase phenocrysts in the groundmass. A few phenocrysts contain composite inclusions formed by mutual attachment of several plagioclase crystals; each of them is characterized by a patchy core (~An50-70) with abundant melt inclusions and an oscillatory zoned mantle (~An45-55) (Fig. 9e). In these crystals, the texture of the cores presents strong similarities with that of the smaller plagioclase inclusions (or cluster of small grains) (Fig. 9a, b, e; Supplementary Table 1). Conversely, most plagioclase phenocrysts present the same complex growth/dissolution textures of the larger (1-2 mm) inclusions (patchy and/or oscillatory zoning, sieve texture, dissolution surfaces, secondary alteration into allophane; Fig. 9f). The chemical composition of the phenocrysts ranges from An50 to An89 (Fig. 9e, f), with variable content of Sr (600-1300 ppm), Eu (1.9-3.9 ppm), and the outer layers have sodic composition (An45-60) and relatively low contents of compatible trace elements (Sr 600-900 ppm, Eu 1.9-3.1 ppm) (Figs. 3, 10; Supplementary Table 1).

5. Discussion

Textural evidence of repeated dissolution and growth events are ubiquitous in the studied K-feldspar megacrysts. Compositional transects across megacrysts highlight repeated variations of compatible trace elements from low-Ba (Ba ~1800 ppm) to high-Ba zones (up to 8800 ppm) with deeply resorbed surfaces related to sharp chemical changes. These crystal textures and characteristic chemical zoning are commonly related to disequilibrium due to recharge events of the shallow magma reservoir by deeper mafic magmas, producing convective dynamics within the systems (e.g., Bateman, 1995; Couch et al., 2001; Ginibre et al., 2002a, 2002b; Huppert et al., 1984; Kahl et al., 2013; Perugini and Poli, 2012; Singer et al., 1995; Turner and Campbell, 1986). The abundance of mafic to intermediate (trachybasalt to latite) microgranular enclaves at Mt. Amiata is field evidence for repeated influxes of hotter magma in the resident trachydacitic magma reservoir.

362

363 *5.1 The origin of the chemical zoning in K-feldspar megacrysts*

364

365 We combined compatible Ba and Sr and semi-compatible Rb trace element contents in K-
366 feldspar, whole rock, and glassy groundmass to retrace the petrogenetic processes occurring in the
367 magmatic system during the growth of the studied K-feldspar megacrysts.

368 The composition of the different layers within the megacrysts was inverted to the melt
369 composition in which the crystal grew, using the formula:

$$C^{\alpha}_{melt} = C^{\alpha}_{Kfel}/Kd^{\alpha}_{Kfel/l}$$

370 where C^{α}_{melt} is the concentration of the α element in the melt (or liquid), C^{α}_{Kfel} is the
371 concentration of the element α in K-feldspar, and $Kd^{\alpha}_{Kfel/l}$ is the partition coefficient. The partition
372 coefficient K-feldspar/melt were calculated using the average composition of the glassy
373 groundmass (table 1) and ten K-feldspar compositions measured in the rims 200 μm thick of the
374 megacrysts, in the samples AMT60 and AMT110, assuming chemical equilibrium between the
375 glassy groundmass and the rim of the crystals. The average Kd (±σ) obtained are $Kd^{Ba}_{Kfel/l} = 8 \pm$
376 2, $Kd^{Rb}_{Kfel/l} = 0.8 \pm 0.02$, $Kd^{Sr}_{Kfel/l} = 5 \pm 0.3$. The calculated compositions of the glass in
377 equilibrium with the different layers within the K-feldspar megacrysts are widely variable, in the
378 range Ba 110-1100 ppm, Sr 130-470 ppm and Rb 340-570 ppm (Fig. 11).

379 Obtained results were compared with fractional crystallization (FC), assimilation plus
380 fractional crystallization (AFC), and magma-mixing (MM) models performed using the
381 PETROMODEL spreadsheet (Ersoy, 2013). The partition coefficients plagioclase/melt ($Kd^{Ba}_{pl/l} =$
382 0.16 ± 0.04 *and* $Kd^{Sr}_{pl/l} = 5 \pm 0.3$) were calculated using the average composition of the glassy
383 groundmass (Table 1) and the composition of the euhedral rims of the phenocrysts (on 9 rim
384 compositions). The partition coefficients between mafic minerals and melt in silicic rocks were
385 taken from the GERM Partition Coefficients Database (https://earthref.org/GERM/). The FC trends

were calculated using the modal proportion of minerals measured in the studied samples (Table 2). The volume percent of each component was transformed in weight percent using a density of 2.5 g/cm^3 for rhyolitic melt and the densities given in the literature for minerals. The AFC process was simulated using the composition of a metasedimentary xenolith (AMT 23 in Conticelli et al., 2015) as assimilant. Shoshonite and andesite enclaves (from Conticelli et al., 2015) were used as mafic end-member in the MM process calculations. All the calculations were performed assuming that the bulk partition coefficient of trace elements remains constant throughout the process. The results of the modelling are reported in Figure 11.

PETROMODEL calculations indicate that the composition of the glassy groundmass cannot be reproduced from the whole rock composition by fractional crystallization. In detail, the analyses of the natural glasses fall above the FC line of descent due to a high Ba and Sr contents (Fig. 11a, b). On the contrary, the composition of the glassy matrices can be successfully modelled by the AFC process involving about 25 wt% of assimilant. AFC is possibly combined with mixing processes during the magma evolution. These results agree with the models proposed in the literature for explaining the petrogenetic evolution of the Mt. Amiata magmas, which include fractional crystallization and magma mixing (Conticelli et al., 2015 and references therein), associated with assimilation of metasedimentary xenoliths (Van Bergen and Barton, 1984). Going deeper into details, from the Rb vs. Sr diagram (Fig. 11a), it emerges that the melt compositions, calculated starting from the high-Ba K-feldspars, fit the mixing lines between rhyolitic melts and mafic magmas. The mafic end member involved in the mixing process is commonly <30 wt% and increases up to 40 wt% for the composition referred to the K-feldspar with higher Sr contents (Fig. 11a). Thus, we suggest that the compositional heterogeneity of the K-feldspar megacrysts may be associated with the extent of hybridization of the melt in which they regrow, within the shallow, trachydacitic magma body that fed the Mt. Amiata volcanic activity.

However, in the Rb vs. Ba diagram (Fig. 11b), the calculated melts fall far above the FC, AFC, and MM trends. Two main factors may be responsible for the anomalous high contents of Ba:

i) the choice of the partition coefficients, and ii) a possible crystal-melt disequilibrium. The choice of the partition coefficients is critical for such kind of modelling. In particular the partition coefficient K-feldspar/liquid for Ba. The value of $Kd^{Ba}_{Kfel/l} = 8$ obtained by crystal/melt equilibrium in this work is consistent with the values commonly used in the silicic rocks (see for example Słaby et al., 2007), but the $Kd^{Ba}_{Kfel/l}$ given in literature cover a broad range of values from 1 to 20-25, depending on the chemical composition of the crystal and the melt and the physical conditions (GERM Partition Coefficients Database; Icenhower and London, 1996; Leeman and Phelps, 1981). If a fairly high value of $Kd^{Ba}_{Kfel/l} = 15$ is used to invert the feldspar composition to the melt in equilibrium, the melt compositions obtained approximate to mixing lines (Fig. 11b), and the extent of hybridization is consistent with that obtained by the Sr contents. However, departure from the equilibrium during magma-mixing can strongly affect the partition coefficients between crystal and liquid (see for example Albarède and Bottinga, 1972; Loomis, 1982; Singer et al., 1995; Arzilli et al., 2018), and non-equilibrium partitioning during magma mixing may induce an enrichment of Ba content rimward of resorption surfaces in K-feldspar megacrysts (Gagnevin at al., 2005). Arzilli et al. (2018) founded that disequilibrium crystal growth in alkali feldspar produces a strong increasing of the partition coefficient of the compatible trace elements (e.g. Ba and Sr), higher growth rates corresponding to higher apparent $Kd^{Ba}_{Kfel/l}$ and $Kd^{Sr}_{Kfel/l}$ values. Accordingly, we argue that disequilibrium phenomena related to dissolution and crystal regrowth are responsible for the anomalous Ba enrichment observed in the studied K-feldspar megacrysts. Likely a relatively low degree of undercooling (lower than 30-50 °C used in the experiments of Arzilli et al., 2018) can produce apparent increasing of the most compatible element (Ba), having a minor effect on Sr. Disequilibrium conditions are also consistent with a fairly high crystal-growth rate inferred by the textural features of the Ba-rich layers and the hosted plagioclases (see discussion below).

The different partitioning of Ba, Rb, and Sr observed in studied K-feldspars (Fig. 8) points to distinct chemical signatures of the melt in which the crystals grew. This indicate that the

chemical zoning in the K-feldspar megacrysts reproduces both the different degree of hybridization of the magmas, and the heterogeneity of the primary mafic magmas that periodically refilled the trachydacitic magma reservoir of Mt. Amiata volcano (Conticelli et al., 2015; Poli and Peccerillo, 2016; Van Bergen, 1985).

The textural and chemical zoning of the dark oscillatory layers (DOL) can reflect the convection within the silicic magma reservoir that repeatedly moves the crystals through zones with variable chemical characteristics and temperature (e.g., Couch et al., 2001; Cox et al., 1996; D'Oriano et al., 2017; Ginibre et al., 2002a, b; Moussallam et al., 2015). Weak dissolution may also be originated from re-heating of the magma induced by the arrival of hotter magma from depth, without physical mixing with the resident trachydacite. The saw-tooth pattern of the zoning is likely enhanced by the discharge during the dissolution of K-feldspar chemical components into the melt adhering to the crystal, and the subsequent crystallization of a K-feldspar in which an initially high-Ba content decreases as growth proceeds (Fig. 6). We rule out that saw-tooth patterns are attributed to a diffusion–controlled growth kinetics at the boundary layer around the growing crystal (Allègre et al. 1981; L'Heureux, 1993), because this growth model produces oscillatory layers on a scale of 10-30 μm, that are much thinner than that observed in the DOL (up to 300 μm).

5.2 Inferences from the plagioclase inclusions

The plagioclase hosted in the megacrysts, as well as many phenocrysts in the groundmass, present a variety of textures, from patchy to direct or oscillatory zoning, and from skeletal to deeply resorbed shapes, and variable chemical composition. The composition of the rims of the phenocrysts, in textural equilibrium with the groundmass glass, is around An50, whereas bytownitic compositions, up to An 89 are largely present in patches and layers within the crystals (both phenocrysts and inclusions).

462 Some An-rich plagioclase cores might represent remnants of metasedimentary xenoliths
463 (Van Bergen and Barton, 1984), but zoning commonly found in the plagioclase, both within the
464 megacrysts and in the groundmass, points to a magmatic origin. Similarly, a xenocrystic origin from
465 mafic magmas is not consistent with the trace element chemistry. As already done for K-feldspar,
466 the composition of the An rich plagioclase (An65-An89) was inverted to the melt composition in
467 which the crystal grew using the content of Sr in plagioclase and $Kd_{pl/l}$ ($C^{Sr}_{melt} = C^{Sr}_{pl}/Kd^{Sr}_{pl/l}$). The
468 partition coefficient for Sr in plagioclase strongly depend on the An component, Sr content
469 decreasing with An content increasing (Blundy and Wood, 1991). Using a $Kd^{Sr}_{pl/l}$ =2 (among the
470 lowest values given in the GERM Partition Coefficient Database) the plagioclase with composition
471 An65-80 is in equilibrium with melts having Sr content of 350-600 ppm, which is lower than that of
472 the enclaves (600-850 ppm, Conticelli et al., 2015). Only few points An84-89 in the cores of the
473 phenocrysts give melt in equilibrium with Sr ~800-900 ppm and have likely a xenocrystic origin.
474 As an alternative, the high An content in the plagioclase An65-80 must be favored by a high water
475 content of the new hotter magma which stabilizes the anorthite component. A rapid growth under
476 high undercooling mostly related to degassing has been proposed as a possible mechanism for the
477 origin of the patchy zoning in igneous plagioclase (e.g., Anderson, 1984; Landi et al., 2004). We
478 speculate that volatile loss during magma mixing, inducing nucleation and rapid growth, may have
479 originated the patchy zoned texture which typifies many small plagioclase inclusions or aggregates
480 of small crystals (e.g., Fig 9a, b) and their chemical variation from An-rich to An-poor
481 compositions. This is also consistent with their shape (skeletal to hopper) which testify a fairly high
482 growth rate (Lofgren, 1974). The small plagioclase inclusions and the clusters of small grains
483 hosted in the K-Feldspar megacrysts likely formed during a single crystallization event promoted by
484 the rapid variations of the magma conditions. The primary evidence supporting this conclusion is
485 the absence of resorption surfaces, or abrupt changes in the chemical composition, which on turn
486 are abundant in the large plagioclase inclusions and phenocrysts. Ultimately, textural data indicate

that crystallization of the small plagioclase inclusions was nearly contemporaneous to (or immediately preceded) the crystallization of the host high-Ba K-feldspar. The unstable magma conditions also participated in causing the chemical disequilibrium in the high-Ba K-feldspar above discussed.

The larger plagioclase inclusions (Fig. 9d) have the same textural and chemical features of most of the plagioclase phenocrysts. They record repeated dissolution and recrystallization events due to refilling and magma mixing at different extent before their trapping.

5.3 The origin of the patchy texture in K-feldspar

The patchy cores of the K-feldspar megacrysts from Mt. Amiata might be derived from events of dissolution and renewed growth of the crystal (either homogeneous or chemically zoned) due to mixing with hotter mafic magma or heating events, as suggested for similar textures both in volcanic (e.g., D'Oriano et al., 2017; Ginibre et al., 2004) and intrusive (e.g., Cox et al., 1996; Gagnevin et al., 2004, 2005; Słaby et al., 2017; Vernon, 1986) igneous rocks. The large pockets of glass present in the cores (e.g., Fig. 5c) are commonly explained as embayments due to dissolution, subsequently sealed by regrowth of the crystal. However, as shown in Fig. 5e, the early formation of aggregates of K-feldspar participated in developing the texture and zoning of the megacrysts cores. During the crystal clustering and growth, melt pockets and grains of minerals were trapped. Post entrapment crystallization on the rims of the melt pockets can give chemical zoning that does not follow the crystal boundary or regular crystal shapes, resulting in a general patchy zoning. Successive events of dissolution and regrowth can further develop the patchy zoning and modify the original texture up to hide the morphology of the early aggregates. The patchy Ba-rich layers within the K-feldspar likely originated by not-equilibrium crystal growth, which was enhanced by spasmodic events induced by magma-mixing.

513 *5.4 Insights into the megacrysts origin*

514

515 Textural and chemical zoning in the K-feldspar megacrysts hosted in the Mt. Amiata
516 effusive products indicate that these crystals grew as phenocrysts in a silicic magma reservoir
517 during repeated dissolution and crystallization events.

518 The K-feldspar dimension in the studied products is however unusual, because most of the
519 silicic effusive products contain K-feldspar phenocrysts, but do not develop large megacrysts. The
520 megacrystic lava dome and *coulées* at Mt. Amiata host a quantity of microgranular magmatic
521 enclaves that is larger than observed in megacryst-free lava flows (Conticelli et al. 2015; Ferrari et
522 al. 1996; Van Bergen et al. 1983), although quantitative data are not yet available. This suggests a
523 correlation between repeated influx of hotter magma from the depth and the formation of the K-
524 feldspar megacrysts.

525 According to Vernon (1986, 2010), the large size of the megacrysts is evidently due to
526 nucleation difficulties for K-feldspar in silicic melts, but we argued that repeated influx of new
527 hotter magma could favour the growth of megacrysts in the trachydacite magmas of Mt. Amiata.
528 The data here presented indicate that reheating during magma mixing increases the temperature of
529 the system above the liquidus temperature of the K-feldspar inducing dissolution. After dissolution,
530 cooling and degassing in the chaotic mixed system moves again the system below the liquidus
531 temperature and crystallization resumes under a certain amount of undercooling. The degree of
532 undercooling for K-feldspar should be low to medium, as discussed in section 5.1. At low/medium
533 undercooling (e.g. 20-40 °C in the experiments carried out by Arzilli and Carroll (2013) on
534 trachytic melts at 100 MPa) growth dominates crystallization process, while nucleation dominates
535 at high undercooling (Fenn, 1977; Arzilli and Carroll, 2013). At low/medium undercooling,
536 heterogeneous nucleation can be favoured because a lower activation energy required respect to
537 homogeneous nucleation (Vernon, 2004, p. 46-51 and reference therein). As a result, after an event
538 of dissolution, crystal kinetics favours the rapid growth of K-feldspar layers (with abundant

539 inclusions of mineral grains and melt) on existing K-feldspars. When equilibrium is restored, the
540 crystal growth of the existing crystals, continue in the convective magma chamber (DOL). In
541 addition, layer discontinuities in the DOL highlight dissolution of about 150 μm of crystal and a
542 thicker portion is possibly resorbed during more disruptive magma-mixing. Thus, small crystals that
543 possibly formed in the trachydacitic magma chamber during cooling and convection, may be totally
544 resorbed during a mixing event. In this view, repeated reheating of the magma chamber can favour
545 the formation of few large crystals rather than abundant small phenocrysts. Higgins (1999, 2011)
546 suggested that megacrysts develop from the host magma by coarsening ("*Ostwald ripening"*)
547 promoted by cycling changes of the temperature in response to the influx of mafic magmas. Based
548 on the textural feature of the megacrysts shown in the present work, crystallization kinetics favored
549 the formation of large aggregates of K-feldspars which can become the nuclei of new megacrysts
550 (Fig.5 e). However, the process that promotes aggregation of few large crystals (mm sized in Fig.
551 5e) appears to be different from the *"Ostwald ripening"* mechanism, which should involve
552 coarsening of a number of small nuclei (or many small crystals). These aggregates can be better
553 explained as *synneusis* structures (Stull, 1979; Vance, 1969), that is mutual attachment of crystals
554 probably related to magmatic turbulence induced by magma mixing and/or convection. Mutual
555 attachment of crystals can be one of the factors that participate in the formation of large megacrysts.
556 A schematic cartoon illustrating the growth mechanisms of the K-feldspar megacrysts is shown in
557 Fig. 12.
558
559 *5.5 Comparison with megacrystic plutons*
560
561 A comparison among theK-feldspar megacrysts of Mt. Amiata and those hosted in intrusive
562 products of the Tuscan Magmatic Provinces (e.g. the monzogranitic Mt. Capanne Pluton, Elba
563 island; Gagnevin et al., 2004, 2005) reveals strong similarities in both the chemical zoning and
564 texture, although a detailed comparison of the chemical zoning is hampered by the formation of

565 pertitic textures in the intrusive K-feldspar. Both plutonic megacrysts from Mt Capanne and
566 volcanic megacrysts from Mt Amiata, highlight repeated dissolution and regrowth episodes,
567 associated with large trace-elements chemical zoning, suggesting a similar growth history. A
568 phenocrystic origin of the K-feldspar megacrysts in plutonic rocks has been widely favoured in the
569 most recent literature. The study of K-feldspar megacrysts from Mt. Amiata and their comparison
570 with ones from Mt. Capanne pluton, also support this interpretation.

571 Mt. Capanne pluton is also characterized by the occurrence of abundant microgranular
572 enclaves with variable composition, and according to Gagnevin et al. (2008), the abundance of
573 megacrysts is positively correlated with the volumetric abundance of the mafic inclusions. As
574 discussed for Mt. Amiata products, this suggests that the repeated influxes of hotter magma into a
575 shallow magma body may favour the growth of the extraordinary large K-feldspar crystals. We
576 argue that reiterated reheating of the silicic magma chamber in which K-feldspar crystallize is one
577 mechanism that can provide thermal conditions for the growth of the large crystals (as also
578 suggested by Moore and Sisson, 2008).

579

580 **6. Conclusions**

581

582 The study of the K-feldspar megacrysts hosted in the trachydacitic lava flows, lava domes
583 and *coulées* of Mt. Amiata evidences a complex crystallization history which was driven by
584 successive disequilibrium and re-equilibration events, due to the influx of hotter magmas and
585 convection in the magma reservoir. Magma mixing events are testified by deeply resorbed surfaces
586 and disequilibrium crystal regrowth. The variable chemical composition of the K-feldspars is
587 related to a different extent of hybridization during magma-mixing, and to chemical heterogeneities
588 characterizing the mafic magmas that refilled the silicic reservoir. Finally, the fairly rapid growth
589 rate inducing chemical disequilibrium was highlighted by the anomalous Ba enrichment rimwards
590 of the resorption surfaces.

We suggest that the K-feldspar megacrysts from Mt. Amiata originate by the interplay of crystal kinetics and repeated reheating due to magma mixing. A single magma mixing event involves reheating and K-feldspar dissolution, during which the microphenocrysts can be resorbed entirely, (ii) after dissolution a low nucleation rate favours heterogeneous crystallization, and a fairly rapid crystal re-growth. After the destabilization events, equilibrium is restored, and the crystals continue to grow under nearly equilibrium conditions in a convective magma chamber, where a low nucleation rate makes difficult the formation of new nuclei. Repeated magma influx and reheating can determine the thermal condition ideal to the growth of these large crystals.

The textural and chemical similarities observed in K-feldspar megacrysts from Mt. Amiata lava domes and *coulées* and Mt. Capanne pluton (Tuscan Magmatic Province) show that megacrysts from these rocks have the same growth history and support the hypothesis of a phenocrystic origin of intrusive K-feldspar megacrysts.

Acknowledgments

Appreciation is extended to L. Marini for his suggestions on the earlier version of manuscript. The Authors are grateful to T. Abebe Adhana for the help during the fieldwork. M. Nazzari is acknowledged for assistance during electron microprobe analyses. SLF wants to thank Annarita Paolillo who helped in some sample preparations. We are grateful to R.H. Vernon and an anonymous reviewer, which provided constructive and thorough reviews that helped us to improve this manuscript. Finally, we are grateful to N. Eby for editorial work and helpful comments. This work was partially financially supported by the Tuscan regional authority (Regione Toscana) in the framework of the LAMMA-CNR Project “Monografia vulcanologica del Monte Amiata” (C.P. responsible).

615 **Figure captions**

616 **Figure 1 –** Synthematic map of Mt. Amiata with the location of the sampling sites (yellow
617 dots). In the legend a comparison between the stratigraphic units recognized by Principe et al.
618 (2017, 2018), Vezzoli and Principe (2017) and the previous stratigraphic subdivisions (Marroni et
619 al., 2015; Ferrari et. al. 1996; Mazzuoli and Pratesi, 1963) is shown.

620 **Figure 2 –** T.A.S. (Total Alkali-Silica) diagram for silicic lava flows and lava domes (light
621 grey dots) and magmatic enclaves (dark grey diamonds). Triangles represent the rocks studied in
622 this work. Data from Rombai et al., 1995; Ferrari et al., 1996; Cristiani and Mazzuoli, 2003;
623 Cadoux and Pinti, 2009; Conticelli et al., 2015; La Felice et al. 2017.

624 **Figure 3** – Feldspar ternary diagram for K-feldspar (both megacrysts >1 cm and phenocrysts
625 and fragments <1 cm) and plagioclase phenocrysts represented in terms of albite (Ab), anorthite
626 (An) and orthoclase (Or) end-members.

627 **Figure 4 –** Examples of K-feldspar megacrysts from Mt. Amiata: (a) megacryst weathered
628 out of the friable vesicular groundmass; (b) megacryst embedded in the groundmass; (c) entire
629 simple prismatic crystal elongated parallel to (010) face; (d) broken megacryst showing internal
630 dusty zone and a most homogeneous external rim.

631 **Figure 5** – Mosaic of BSE (a1) and CL (a2, b, c, d, e) images of K-feldspar megacrysts
632 showing the textural features mentioned in the text. Crystals are cut through the approximate
633 geometric centre and nearly perpendicular (a) or parallel (b, c, d) to (010). a) Comparison between
634 images obtained with BSE (a1, left half) and CL (a2, right half) detectors. The rectangles indicate
635 the overlap area; a), b), c) images show the typical dusty internal portions formed by a large patchy
636 zoned core surrounded by several zoned layers with rounded to resorbed boundaries and concentric
637 alignments of mineral grains; d) a relatively small crystal composed by a patchy zoned core
638 crowded with melt inclusions, vesicles and mineral grains, surrounded by a concentric, oscillatory
639 zoned corona; e) the megacryst is formed by clustering of several crystals (e.g. A, B, C), as shown
640 by angular discordances of the growth layers. The shape of the megacryst is determined by the post

641 aggregation overgrowth. DOL= dark oscillatory layers. Dashed line indicates the boundary between
642 different zones as indicate in the text. Arrows indicate resorption surfaces.
643 A high-resolution version of the images is available as Virtual Microscope (eSlide VM…) (or
644 supplementary material)

645 **Figure 6 –** Enlargement of the corner at the bottom left of the Figure 5d. The CL image
646 illustrates the oscillatory textures in DOL (dark oscillatory layers). Arrows indicate resorption
647 surfaces. The numbers are Ba ppm content.

648 **Figure 7 –** (a), (b), (c) Ba and Sr (ppm) rim to core profiles across selected K-feldspar
649 megacrysts. CL images are parts of K-feldspar megacrysts in Figure 5.

650 **Figure 8 –** Or mol% vs. Rb ppm (a) and selected trace elements binary diagrams (b-f) for K-
651 feldspar megacrysts.

652 **Figure 9 –** Plagioclase inclusions in K-Feldspar megacrysts AMT 60_cr2 (a, b, c,), AMT
653 110_cr2 (d) and plagioclase phenocrysts from AMT110 (e, f). (a, b) plagioclase clusters (CL
654 images) formed by aggregation of more grains. Large irregular melt pockets are embedded during
655 the crystal growth; (c) BSE images of a plagioclase inclusion with direct chemical zoning; (d) BSE
656 images show patchy zoned cores (An50-An77) encircled by a mantle with oscillatory zoning and
657 corroded surfaces; (e) CL image of a plagioclase phenocryst composed by a main crystal and at
658 least three smaller euhedral grains attached. They are characterized by patchy zoned cores with
659 large melt inclusions and bubbles, encircled by oscillatory zoned mantles; (f) the BSE image
660 display a plagioclase phenocryst with sieve texture and extensive patchy zoning. The An 85 zones
661 are altered into allophane. Single numbers are An mol%; double numbers are An mol% and Ba ppm
662 (An-Ba).

663 **Figure 10 –** An mol% vs. Sr ppm (a) and Eu ppm vs. Sr ppm (b) binary diagrams for
664 plagioclase inclusions and phenocrysts**.**

665 **Figure 11 –** Binary plots Rb vs. Sr (a) and Rb vs. Ba (b) showing the results of geochemical
666 modeling for fractional crystallization (FC), assimilation and fractional crystallization (AFC) and

667 magma mixing (MM) processes (Ersoy, 2013). See text for explanation. Diamonds: micaceous
668 (filled) and andesitic (empty) enclaves from Conticelli et al. (2015); Square: metasedimentary
669 xenolith from Conticelli et al. (2015); triangles: whole rock composition from La Felice et al.
670 (2017); large circle: groundmass glass composition.
671 **Figure 12** – Schematic cartoon illustrating the growth mechanisms of the K-feldspar megacrysts.
672 (a) Nucleation and growth of few crystals in trachydacite magma. Mutual attachment of crystals can
673 form crystal aggregates; (b) magma mixing and reheating induce dissolution of the K-feldspars; the
674 smallest crystals can be totally resorbed; (c) temperature decrease and degassing during mixing
675 promote a new event of crystallization: patchy cores form and a Ba-rich patchy corona with
676 abundant mineral inclusions growths; (d) the system re-equilibrate after mixing event and an
677 oscillatory corona growth in a convective magma body. A low nucleation rate hampers the growth
678 of new crystals. New dissolution and regrowth cycles result from reiterated magma influxes.
679
680 **Table 1** – Major and trace elements composition of whole rocks from La Felice et al. (2017)
681 and groundmass glasses (this work). bdl= below detection limit.
682 **Table 2** – Modal analyses in vol% of phenocrysts in the analyzed samples. Abbreviations:
683 plg=plagioclase; K-fel=K-feldspar; opx=orthopyroxene; cpx=clinopyroxene; bt=biotite; ox=Fe-Ti
684 oxydes; qtz=quartz; gdm= groundmass.
685 **Supplementary Table 1 –** Major and trace element compositions of K-Feldspar (a) and
686 plagioclase (b).
687
688

689 **References**

690

691 Albarède, F., Bottinga, Y., 1972. Kinetic disequilibrium in trace element partitioning between
692 phenocrysts and host lava. Geochimica et Cosmochimica Acta 36, 141-156.

693 Allègre, C.J., Provost, A., Jaupart, C., 1981. Oscillatory zoning: a pathological case of crystal
694 growth. Nature 294, 223-229.

695 Anderson, A.T., 1984. Probable relations between plagioclase zoning and magma dynamics, Fuego
696 volcano, Guatemala. American Mineralogist 69, 660-676.

697 Arzilli, F., Carroll, M.R., 2013. Crystallization kinetics of alkali feldspars in cooling and
698 decompression-induced crystallization experiments in trachytic melt. Contribution to
699 Mineralogy and Petrolology 166, 1011–1027.

700 Arzilli, F., Fabbrizio, A., Schmidt, M.W., Petrelli, M., Maimaiti, M., Dingwell, D.B., Paris, E.,
701 Burton, M., Carroll, M.R., 2018. The effect of diffusive re-equilibration time on trace element
702 partitioning between alkali feldspar and trachytic melts. Chemical Geology 495, 50–66.

703 Balducci, S., Leoni, L., 1981. Sanidine megacrysts from M. Amiata trachytes and Roccastrada
704 Rhyolites. Neues Jahrbuch für Mineralogie-Abhandlungen 143, 15-36.

705 Bateman, R., 1995. The interplay between crystallization, replenishment and hybridization in large
706 felsic magma chambers. Earth Sciences Reviews 39, 91-106.

707 Blundy, J.D., Wood, B. J., 1991. Crystal-chemical controls on the partitioning of Sr and Ba between
708 plagioclase feldspar, silicate melts, and hydrothermal solutions. Geochimica et Cosmochimica
709 Acta 55, 193-209.

710 Cadoux A., Pinti D.L., 2009. Hybrid character and pre-eruptive events of Mt. Amiata volcano (Italy)
711 inferred from geochronological, petro-geochemical and isotopic data. Journal of Volcanology
712 and Geothermal Research 179, 169–190.

713 Cherniak, D.J., 2002. Ba diffusion in feldspar. Geochimica et Cosmochimica Acta 66, 1641–1650.

714 Conticelli, S., Boari, E., Burlamacchi, L., Cifelli, F., Moscardi, F., Laurenzi, M.A., Ferrari Pedraglio,
715 L., Francalanci, L., Benvenuti, M.G., Braschi, E., Manetti P., 2015. Geochemistry and Sr-Nd-
716 Pb isotopes of Monte Amiata Volcano, Central Italy: evidence for magma mixing between
717 high-K calc-alkaline and leucititic mantle-derived magmas. Italian Journal of Geosciences
718 134, 268-292.
719 Couch, S., Sparks, R.S.J., Carroll, M.R., 2001. Mineral disequilibrium in lavas explained by
720 convective self-mixing in open magma chambers. Nature 411, 1037-1039.
721 Cox, R.A., Dempster, T.J., Bell, B.R., Rogers, G., 1996. Crystallization of the Shap Granite:
722 evidence from zoned K-feldspar megacrysts. Journal of the Geological Society London 153,
723 625-635.
724 Cristiani, C., Mazzuoli, R., 2003. Monte Amiata volcanic products and their inclusions. Periodico di
725 Mineralogia 72, 169-181.
726 D'Oriano, C., Landi, P., Pimentel, A., Zanon, V., 2017. Magmatic processes revealed by
727 anorthoclase textures and trace element modelling: the case of the Lajes Ignimbrite
728 eruption (Terceira Island, Azores). Journal of Volcanology and Geothermal Research
729 347, 44-63.
730 Ersoy, E.Y., 2013. PETROMODELER (Petrological Modeler): a Microsoft® Excel© spreadsheet
731 program for modelling melting, mixing, crystallization and assimilation processes in
732 magmatic systems. Turkish Journal of Earth Sciences 22, 115-125.
733 Fenn, P.M., 1977. The nucleation and growth of alkali feldspars from hydrous melts. The Canadian
734 Mineralogist 15, 135-161.
735 Ferrari, L., Conticelli, S., Burlamacchi, L., Manetti, P., 1996. Volcanological Evolution of the Monte
736 Amiata Volcanic Center, Southern Tuscany, Central Italy: New Geological and Petrochemical
737 data. Acta Vulcanologica 8, 41-56.

738 Gagnevin, D., Daly, J.S., Poli, G., 2004. Petrographic, geochemical and isotopic constraints on
739 magma dynamics and mixing in the Miocene Monte Capanne monzogranite (Elba Island,
740 Italy). Lithos 78, 157-195.
741 Gagnevin, D., Daly, J.S., Poli, G., 2008. Insights into granite petrogenesis from quantitative
742 assessment of the field distribution of enclaves, xenoliths and K-feldspar megacrysts in the
743 Monte Capanne pluton, Italy. Mineralogical Magazine 72, 925–940.
744 Gagnevin, D., Daly, J.S., Poli, G., Morgan, D., 2005. Microchemical and Sr isotopic investigation of
745 zoned K-feldspar megacrysts: insights into the petrogenesis of a granitic system and
746 disequilibrium crystal growth. Journal of Petrology 46, 1689–1724.
747 Ginibre, C., Kronz, A., Wörner, G., 2002a. High-resolution quantitative imaging of plagioclase
748 composition using accumulated backscattered electron images: new constraints on oscillatory
749 zoning. Contribution to Mineralogy and Petrology 142, 436-448.
750 Ginibre, C., Wörner, G., Kronz, A., 2002b. Minor- and trace-elements zoning in plagioclase:
751 implications for magma chamber processes at Parinacota volcano, northern Chile.
752 Contribution to Mineralogy and Petrology 143, 300-315.
753 Ginibre, C., Wörner, G., Kronz, A., 2004. Structure and dynamics of the Laacher See magma
754 chamber (Eifel, Germany) from major and trace element zoning in sanidine: a
755 cathodoluminescence and electron microprobe study. Journal of Petrology 45, 2197-2223.
756 Giraud, A., Dupuy, C., Dostal, J., 1986. Behavior of trace elements during magmatic processes in the
757 crust: application to acidic volcanic rocks of Tuscany (Italy). Chemical Geology 57, 269-288.
758 Glazner, A.F., Johnson, B.R., 2013. Late crystallization of K-feldspar and the paradox of megacrystic
759 granites. Contribution to Mineralogy and Petrology 166, 777-799.
760 Higgins, M.D., 1999. Origin of megacrysts in granitoids by textural coarsening: a crystal size
761 distribution (CSD) study of microcline in the Cathedral Peak Granodiorite, Sierra Nevada,
762 California, in: Castro, A., Fernandez, C., Vigneresse, J.L. (Eds), Understanding Granites:

763 Integrating New and Classical Techniques. Geological Society London Special Publication
764 168, pp. 207-219.
765 Higgins, M.D., 2011. Quantitative petrological evidence for the origin of K-feldspar megacrysts in
766 dacites from Taapaca volcano, Chile. Contribution to Mineralogy and Petrology 162, 709–
767 723.
768 Huppert, H.E., Stephen, R., Sparks, J., Turner, J.S., 1984. Some effects of viscosity on the dynamics
769 of replenished magma chambers. Journal of Geophysical Research: Solid Earth 89, 6857-
770 6877.
771 Icenhower, J., London, D., 1996. Experimental partitioning of Rb, Cs, Sr, and Ba between alkali
772 feldspar and peraluminous melt. American Mineralogist 81, 719-734.
773 Johnson, B.R., Glazner, A.F., 2010. Formation of K-feldspar megacrysts in granodioritic plutons by
774 thermal cycling and late-stage textural coarsening. Contribution to Mineralogy and Petrology
775 159, 599–619.
776 Kahl, M., Chakraborty, S., Pompilio, M., Costa, F., 2013. Constraints on the nature and evolution of
777 the magma plumbing system of Mt. Etna volcano (1991–2008) from a combined
778 thermodynamic and kinetic modelling of the compositional record of minerals. Journal of
779 Petrology 56, 2025–2068.
780 La Felice, S., Abebe, A.T., Principe, C., Vezzoli, L.M., 2017. Caratteristiche petrochimiche delle
781 vulcaniti di Monte Amiata in relazione alla stratigrafia, in: Principe, C., Lavorini, G., Vezzoli,
782 L.M. (Eds.), Il vulcano di Monte Amiata. Edizioni Scientifiche e Artistiche, Nola, pp. 169-
783 191. ISBN 978-88-99742-32-4
784 Landi, P., Métrich, N., Bertagnini, A., Rosi, M., 2004. Dynamics of magma mixing and degassing
785 recorded in plagioclase at Stromboli (Aeolian Archipelago, Italy). Contribution to Mineralogy
786 and Petrology 147, 213-227.

787 Laurenzi, M.A., Braschi, E., Casalini, M., Conticelli, S., 2015. New ^{40}Ar-^{39}Ar dating and revision of
788 the geochronology of the Monte Amiata volcano, central Italy. Italian Journal of Geosciences
789 134, 255-265.
790 Leeman, W.P., Phelps, D.W., 1981. Partitioning of Rare Earths and other trace elements between
791 sanidine and coexisting volcanic glass. Journal of Geophysical Research 86, 10193-10199.
792 L'Heureux, I., 1993. Oscillatory zoning in crystal growths: a constitutional undercooling mechanism.
793 Physical Review E 48, 4460-4469.
794 Lofgren, G., 1974. An experimental study of plagioclase crystal morphology: isothermal
795 crystallization. American Journal of Science 274, 243-273.
796 Loomis, T.P., 1982. Numerical simulations of crystallization processes of plagioclase in complex
797 melts: the origin of major and oscillatory zoning in plagioclase. Contribution to Mineralogy
798 and Petrology 81, 219-229.
799 Marroni, M., Moratti, G., Costantini, A., Conticelli, S., Benvenuti, M.G., Pandolfi, L., Bonini, M.,
800 Cornamusini, G. Laurenzi, M.A., 2015. Geology of the Monte Amiata region, Southern
801 Tuscany, Central Italy. Italian Journal of Geosciences, 134, 200-218.
802 Mazzuoli, R., Pratesi, M., 1963. Rilevamento e studio chimico-petrografico delle rocce vulcaniche
803 del Monte Amiata. Atti della Società Toscana di Scienze Naturali, Memorie Serie A, 70, 355-
804 429.
805 Moore, J.G., Sisson, T.W., 2008. Igneous phenocrystic origin of K-feldspar megacrysts in granitic
806 rocks from the Sierra Nevada batholith. Geosphere 4, 387-400.
807 Moussallam, Y., Oppenheimer, C., Scaillet, B., Buisman, I., Kimball, C., Dunbar, N., Burgisser, A.,
808 Schipper, C.I., Andújar, J., Kyle, P., 2015. Megacrystals track magma convection between
809 reservoir and surface. Earth and Planetary Science Letters 413, 1–12.
810 Paterson, S.R., Vernon, R.H., 2002. Igneous origin of K-feldspar megacrysts in deformed granite of
811 the Papoose Flat Pluton, California, USA. Electronic Geosciences 7, 31–39.

812 Paton C., Hellstrom J., Paul B., Woodhead J., Hergt J., 2011. Iolite: Freeware for the visualization
813 and processing of mass spectrometric data. Journal of Analytical Atomic Spectrometry 26,
814 2508-2518.
815 Pearce J.G.N., Perkins W.T., Westgate J.A., Gorton M.P., Jackson S.E., Neal C.R., Chenery S.P.,
816 1997. A compilation of new and published major and trace element data for NIST SRM 610
817 and NIST SRM 612 glass reference materials. Geostandards Newsletter 21, 115-144.
818 Peccerillo, A., Conticelli, S., Manetti, P., 1987. Petrological characteristics and the genesis of Recent
819 magmatism of Southern Tuscany and Northern Latium. Periodico di Mineralogia 56, 157-172.
820 Peccerillo, A., 2017. Cenozoic Volcanism in the Tyrrhenian Sea Region. Springer (399 pp.).
821 Perini, G., Tepley, F. J., III, Davidson, J. P. & Conticelli, S. (2003). The origin of K-feldspar
822 megacrysts hosted in alkaline potassic rocks from post-orogenic setting: a track for low-
823 pressure processes in mafic magmas. Lithos 66, 223–240.
824 Perugini, D., Poli, G., 2012. The mixing of magmas in plutonic and volcanic environments:
825 Analogies and differences. Lithos 153, 261-277.
826 Petrelli, M., Morgavi, D., Vetere, F.P., Perugini, D., 2016a. Elemental imaging and petro-
827 volcanological applications of an improved Laser Ablation Inductively Coupled Quadrupole
828 Plasma Mass Spectrometry. Periodico di Mineralogia 85, 25-39.
829 Petrelli, M., Laeger K. & Perugini D., 2016b. High spatial resolution trace element determination of
830 geological samples by laser ablation quadrupole plasma mass spectrometry: implications for
831 glass analysis in volcanic products. Geoscience Journal 20, 851-863.
832 Poli, G., Frederick, A., Ferrara, G., 1984. Geochemical characteristics of the south Tuscany (Italy)
833 volcanic province. Constraints on lava petrogenesis. Chemical Geology 43, 203-221.
834 Poli, G., Peccerillo, A., 2016. The Upper Miocene magmatism of the island of Elba (Central Italy):
835 compositional characteristics, petrogenesis and implications for the origin of the Tuscan
836 Magmatic Province. Mineralogy and Petrology 110, 421-445.

837 Principe, C., Vezzoli, L.M., La Felice, S., 2017. Stratigrafia ed evoluzione geologica del vulcano di
838 Monte Amiata, in: Principe, C., Lavorini, G., Vezzoli, L.M. (Eds,), Il vulcano di Monte
839 Amiata. Edizioni Scientifiche e Artistiche, Nola, pp. 169-191. ISBN 978-88-99742-32-4.
840 Principe, C., Vezzoli, L.M., La Felice S., 2018. Geology of Monte Amiata volcano (Southern
841 Tuscany). Alpine and Mediterranean Quaternary (Quaternary: Past, Present, Future - AIQUA
842 Conference, Florence, 13-14/06/2018), 31, 235-238Rombai, C., Trua, T., Matteini, M., 1995.
843 Metamorphic xenoliths and magmatic inclusions in the Quaternary lavas of Mt. Amiata
844 (Tuscany, Central Italy). Inferences for P-T conditions of magma chamber. Atti della Società
845 Toscana di Scienze Naturali Serie A, 102, 21-38.
846 Schindelin, J., Arganda-Carreras, I., Frise, E., et al., 2012. Fiji: an open-source platform for
847 biological-image analysis. Nature Methods 9, 676–682.
848 Singer, B.S., Dungan, M.A., Layne, G.D., 1995. Textures and Sr, Ba, Mg, Fe, K and Ti
849 compositional profiles in volcanic plagioclase: clues to the dynamics of calc-alkaline magma
850 chambers. American Mineralogist 80, 776-798.
851 Słaby, E., De Campos, C.P., Majzner K., Simon, K., Gros, K., Moszumańska, I., Jokubauskas, P.,
852 2017. Feldspar megacrysts from the Santa Angélica composite pluton -
853 Formation/transformation path revealed by combined CL, Raman and LA-ICP-MS data.
854 Lithos 277, 269–283.
855 Słaby, E., Galbarczyk-Gąsiorowska, L., Seltmann, R., Müller, A., 2007. Alkali feldspar megacryst
856 growth: Geochemical modelling. Mineralogy and Petrology 89, 1-29.
857 Słaby, E., Götze, J.,Wörner, G., Simon, K.,Wrzalik, R., Śmigielski, M., 2008. K-feldspar phenocrysts
858 in microgranular magmatic enclaves: a cathodoluminescence and geochemical study of
859 crystal growth as a marker of magma mingling dynamics. Lithos 105, 85–97.
860 Stull, R.J., 1979. Mantled feldspar and synneusis. American Mineralogist 64, 514-518.
861 Turner, J.S., Campbell, I.K., 1986. Convection and mixing in magma chambers. Earth Sciences
862 Reviews 23, 255-352.

863 Van Bergen, M.J., 1985. Common trace elements characteristics of Crustal- and Mantle-derived K-
864 rich magmas at Mt. Amiata (Central Italy). Chemical Geology 48, 125-135.
865 Van Bergen, M.J., Barton, M., 1984. Complex interaction of aluminous metasedimentary xenoliths
866 and siliceous magma; an example from Mt. Amiata (Central Italy). Contribution to
867 Mineralogy and Petrology 86, 374-385.
868 Van Bergen, M.J., Ghezzo, C., Ricci, C.A., 1983. Minette inclusions in the rhyodacitic lavas of Mt.
869 Amiata (Central Italy). Mineralogical and chemical evidence of mixing between Tuscan and
870 Roman type magmas. Journal of Volcanology and Geothermal Research 19, 1-35.
871 Vance, J.A., 1969. On Synneusis. Contribution to Mineralogy and Petrology 24, 7-29.
872 Vernon, R.H., 1986. K-feldspar megacrysts in granites - Phenocrysts, not porphyroblasts. Earth-
873 Science Reviews 23, 1-63.
874 Vernon, R. H., 2004. A Practical Guide to Rock Microstructure. Cambridge University Press.
875 Vernon, R.H., 2010. Granites really are magmatic: using microstructural evidence to refute some
876 obstinate hypotheses, in: Forster, M.A., Fitz Gerald, J.D. (Eds.), Journal of Virtual Explorer
877 35, paper 1.
878 Vernon, R.H., Paterson, S.R., 2008. How late are K-feldspar megacrysts in granites? Lithos 104,
879 327–336.
880 Vezzoli, L.M., Principe, C., 2017. Facies vulcaniche e meccanismi di messa in posto delle vulcaniti
881 del Monte Amiata, in: Principe, C., Lavorini, G., Vezzoli, L.M. (Eds,), Il vulcano di Monte
882 Amiata. Edizioni Scientifiche e Artistiche, Nola, pp. 195-213. ISBN 978-88-99742-32-
883 4.Wilson S.A., 1997. The collection, preparation, and testing of USGS reference material
884 BCR-2, Columbia River, Basalt. U.S. Geological Survey Open-File Report 98.
885

Figure1

Click here to download high resolution image

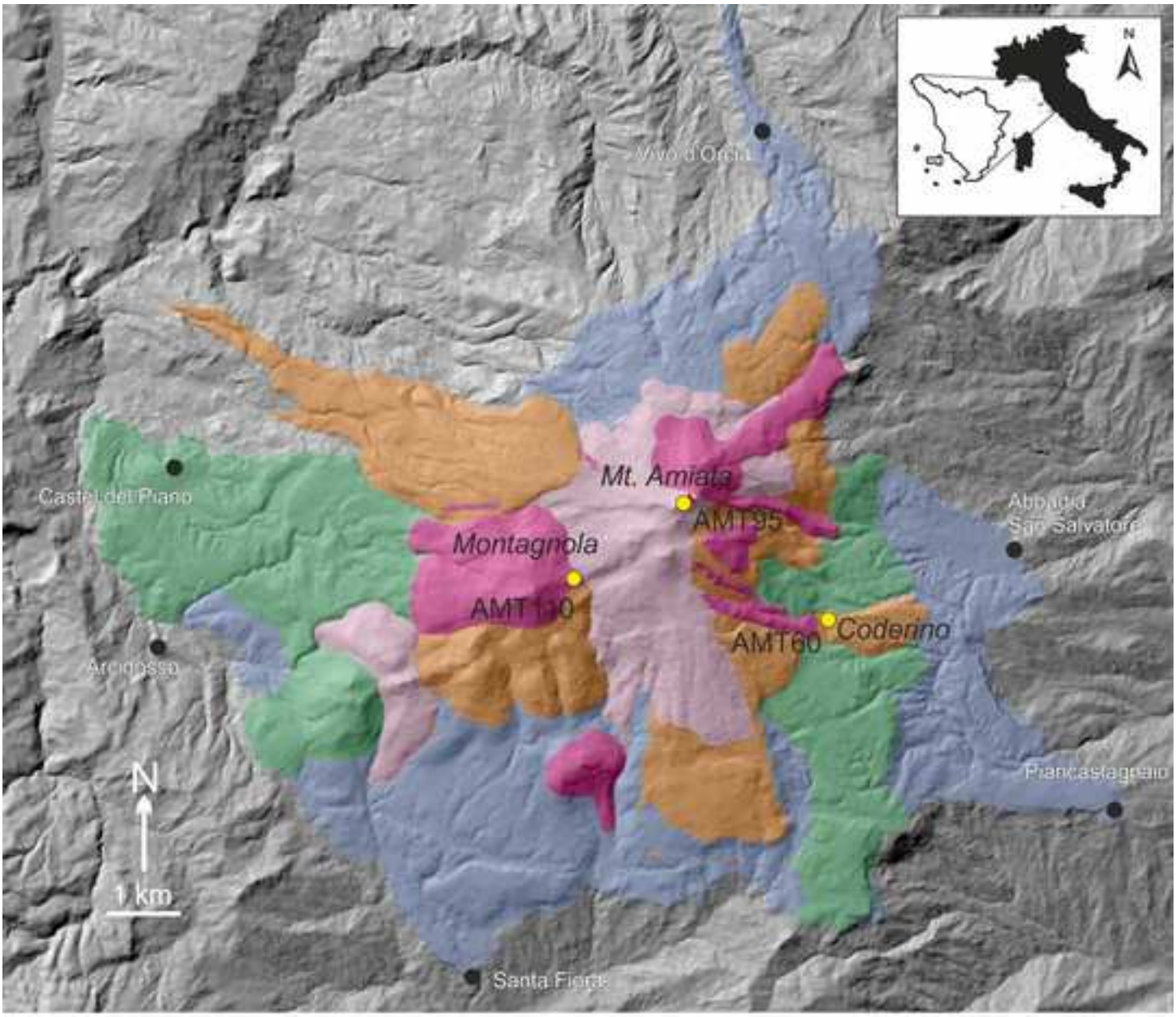

Principe et al. (2017, 2018) *Vezzoli and Principe (2017)*	*Marroni et al. (2015)* * $^{40}Ar/^{39}Ar$ ages from Laurenzi et al. (2015)	*Ferrari et al. (1996)*	*Mazzuoli and Pratesi (1963)*
Monte Amiata Synthem Prato della Contessa Subsynthem Madonna degli Scout Subsynthem Valle Gelata Subsynthem	**Olivine Latite Final Lavas** (231 ka *)	**Olivine Latitic Lava flows**	**Trachytic Lava flows**
	Dome and Massive Lava Flow Complex (301-294 ka *)	**Domes and Lava flows Complex**	**Quartz-latitic Complex B**
Bágnore Synthem Monteaniooso Subsynthem Bagnólo Subsynthem	**Basal Trachydacitic Complex**	**Basal Trachydacitic Complex** Upper unit Lower unit	**Quartz-latitic Lava flows** **Quartz-latitic Complex A**

Figure2

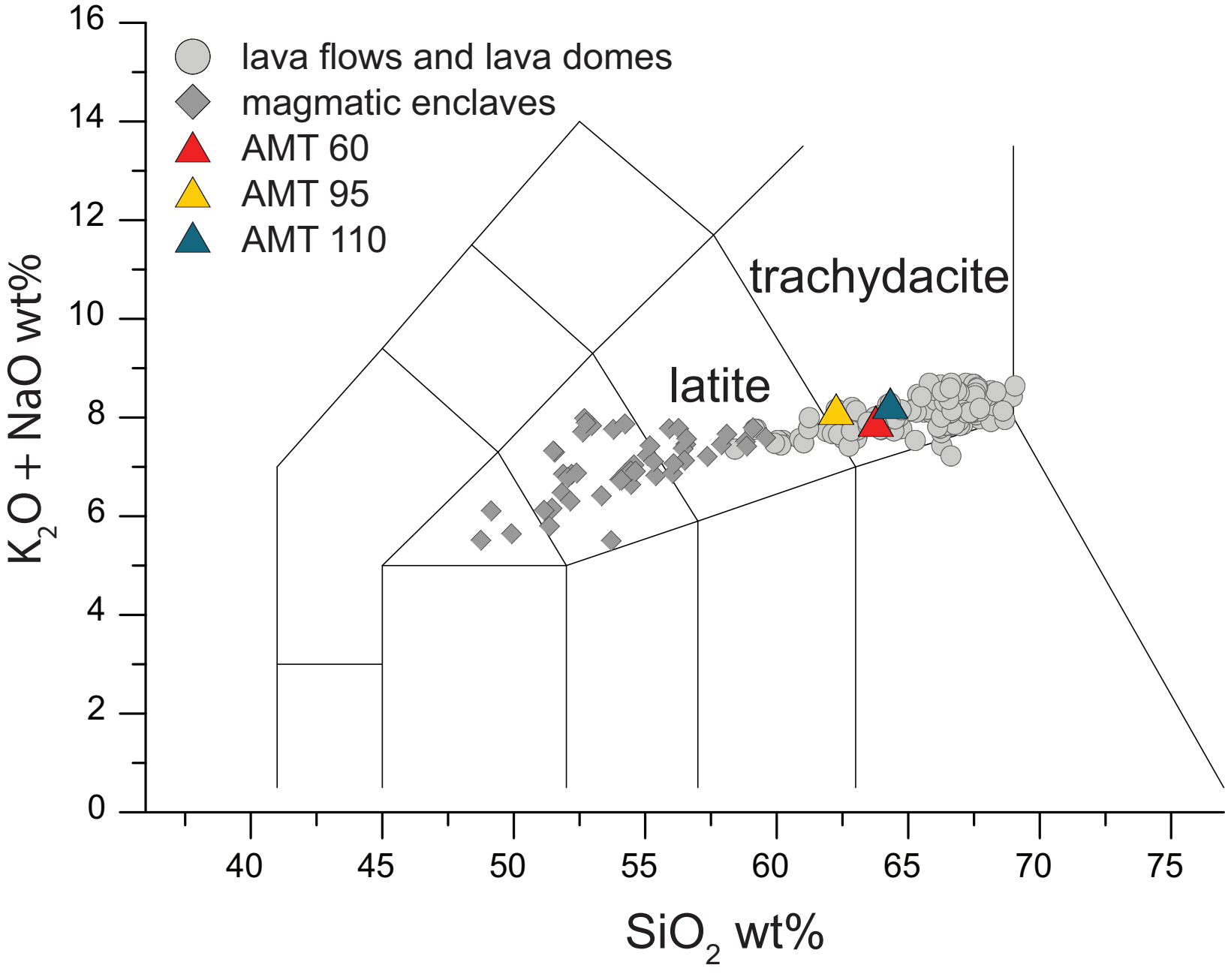
lava flows and lava domes
magmatic enclaves
AMT 60
AMT 95
AMT 110
trachydacite
latite
16
14
12
10
8
6
4
2
0
40
45
50
55
60
65
70
75
K2O + NaO wt%
SiO2 wt%

Figure3

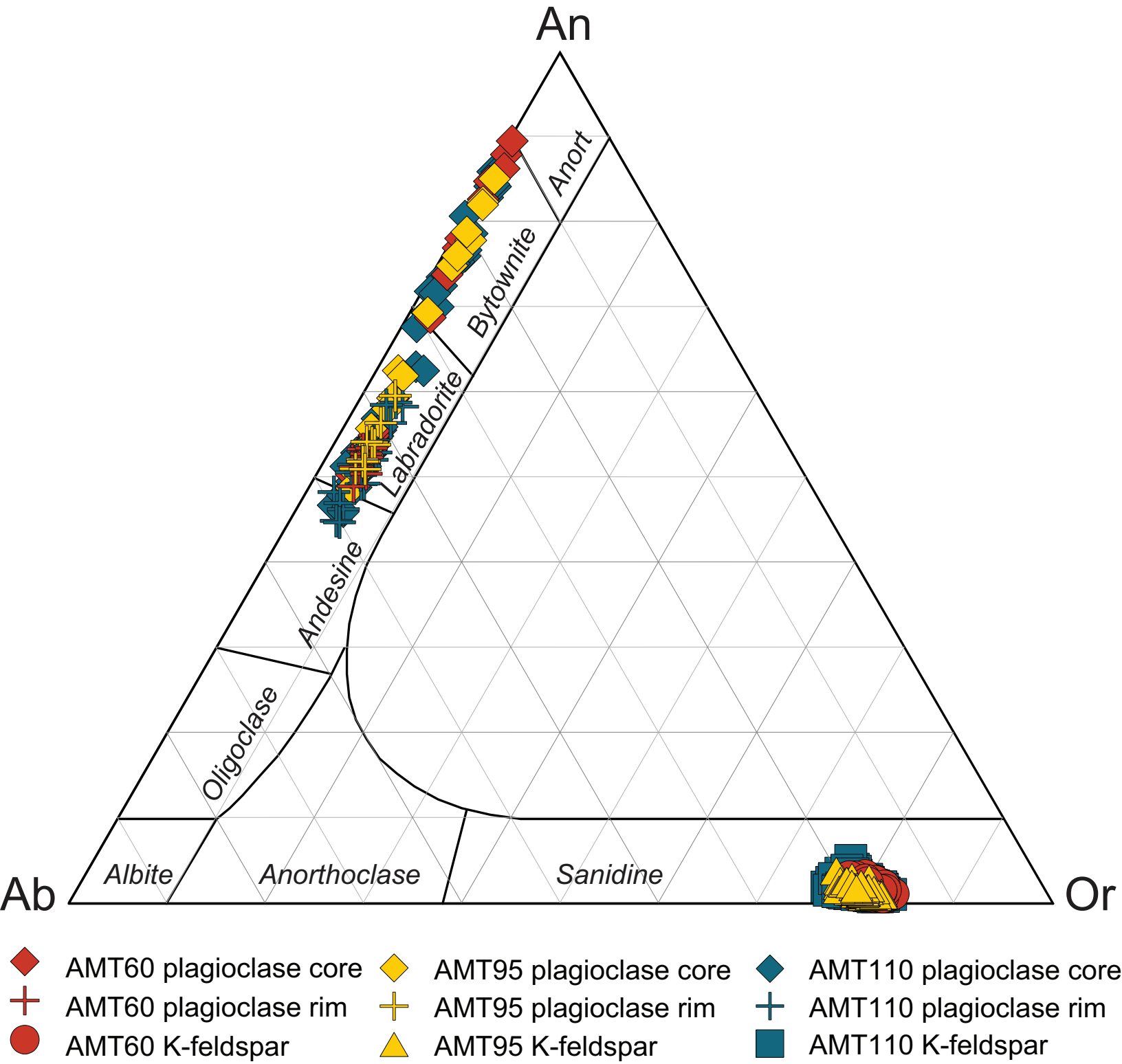
An
Ab
Or
Anort
Bytownite
Labradorite
Andesine
Oligoclase
Albite
Anorthoclase
Sanidine
AMT60 plagioclase core
AMT60 plagioclase rim
AMT60 K-feldspar
AMT95 plagioclase core
AMT95 plagioclase rim
AMT95 K-feldspar
AMT110 plagioclase core
AMT110 plagioclase rim
AMT110 K-feldspar

Figure4

Click here to download high resolution image

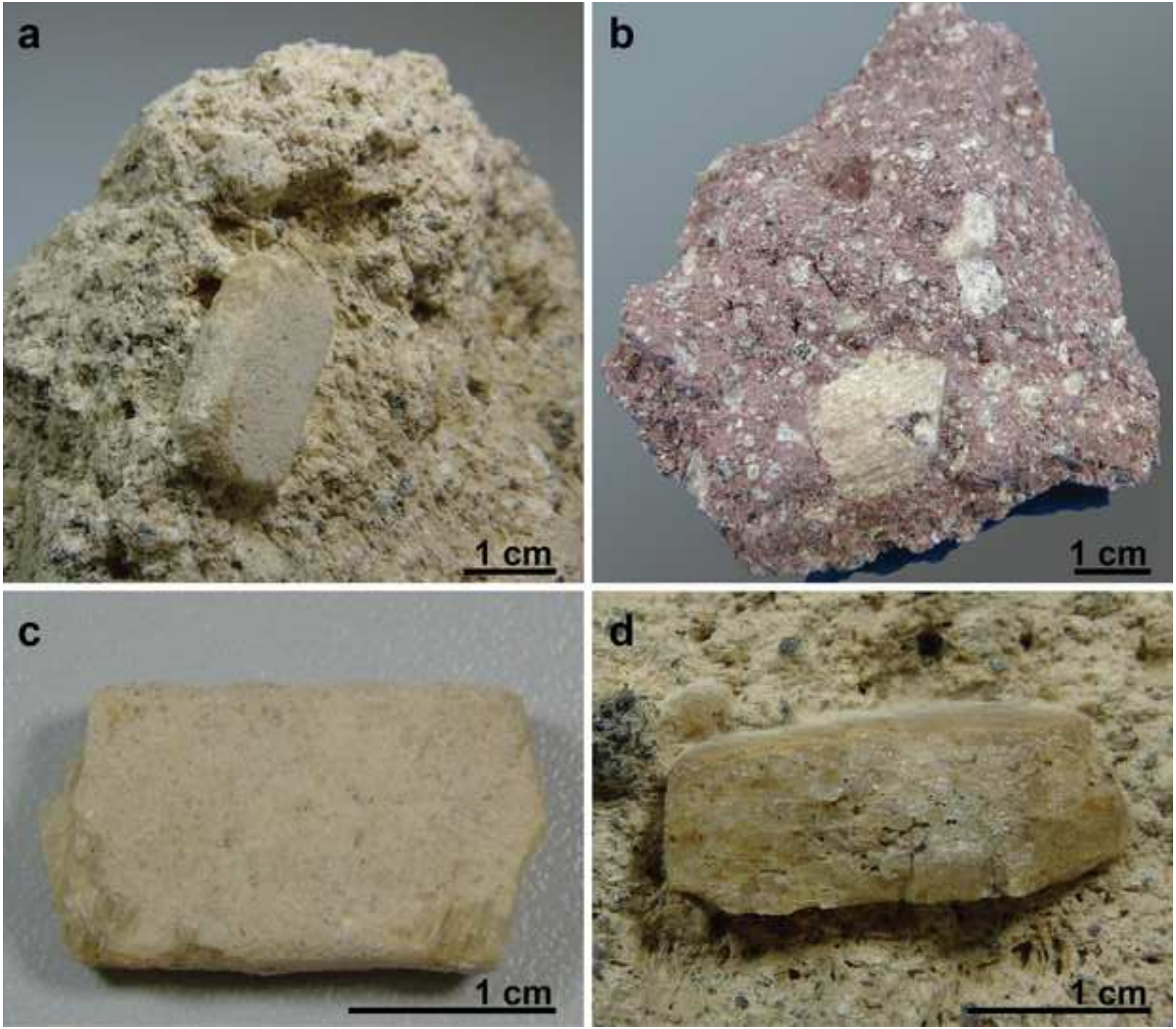

Figure5
Click here to download high resolution image

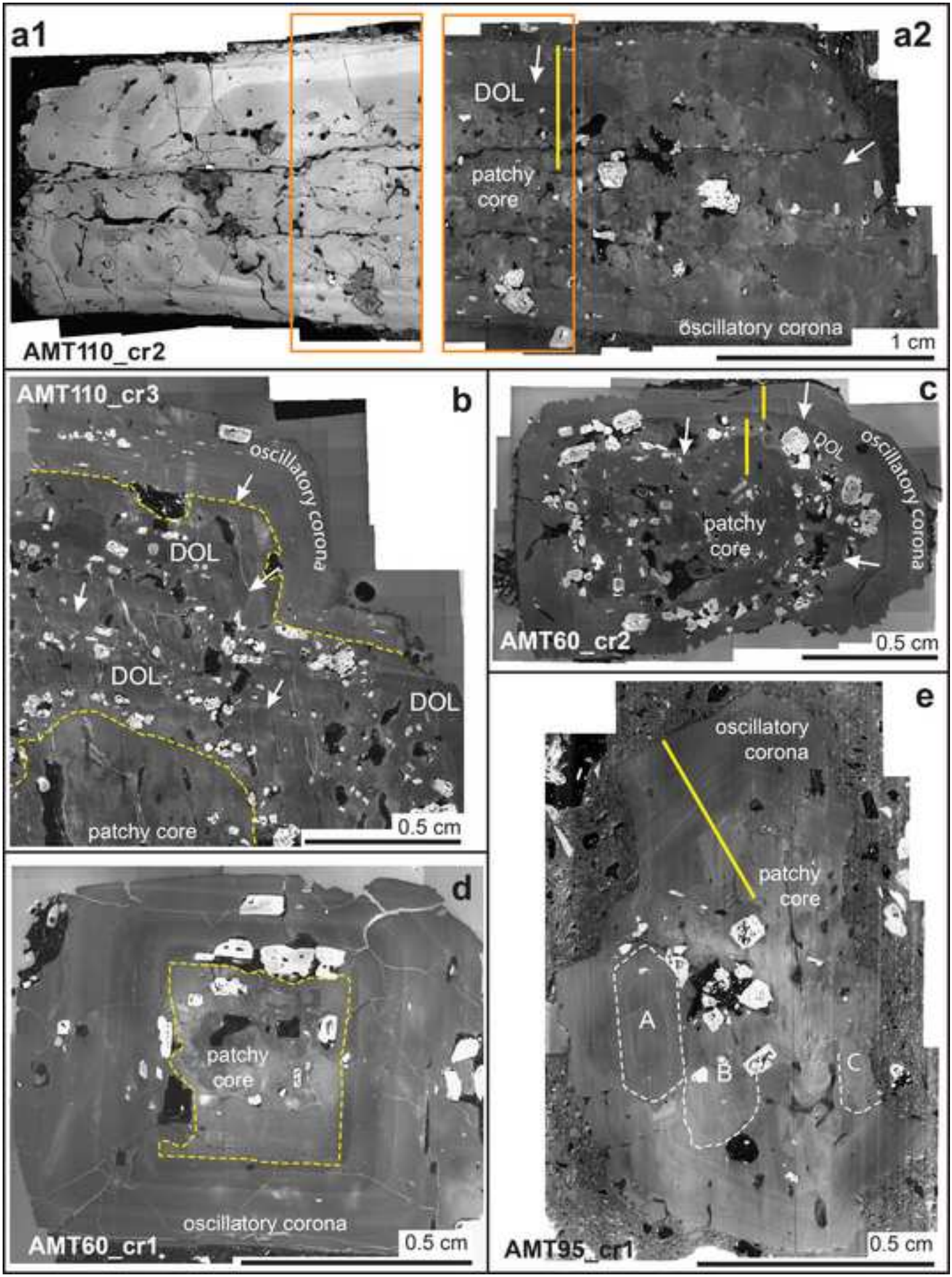

Figure6

Click here to download high resolution image

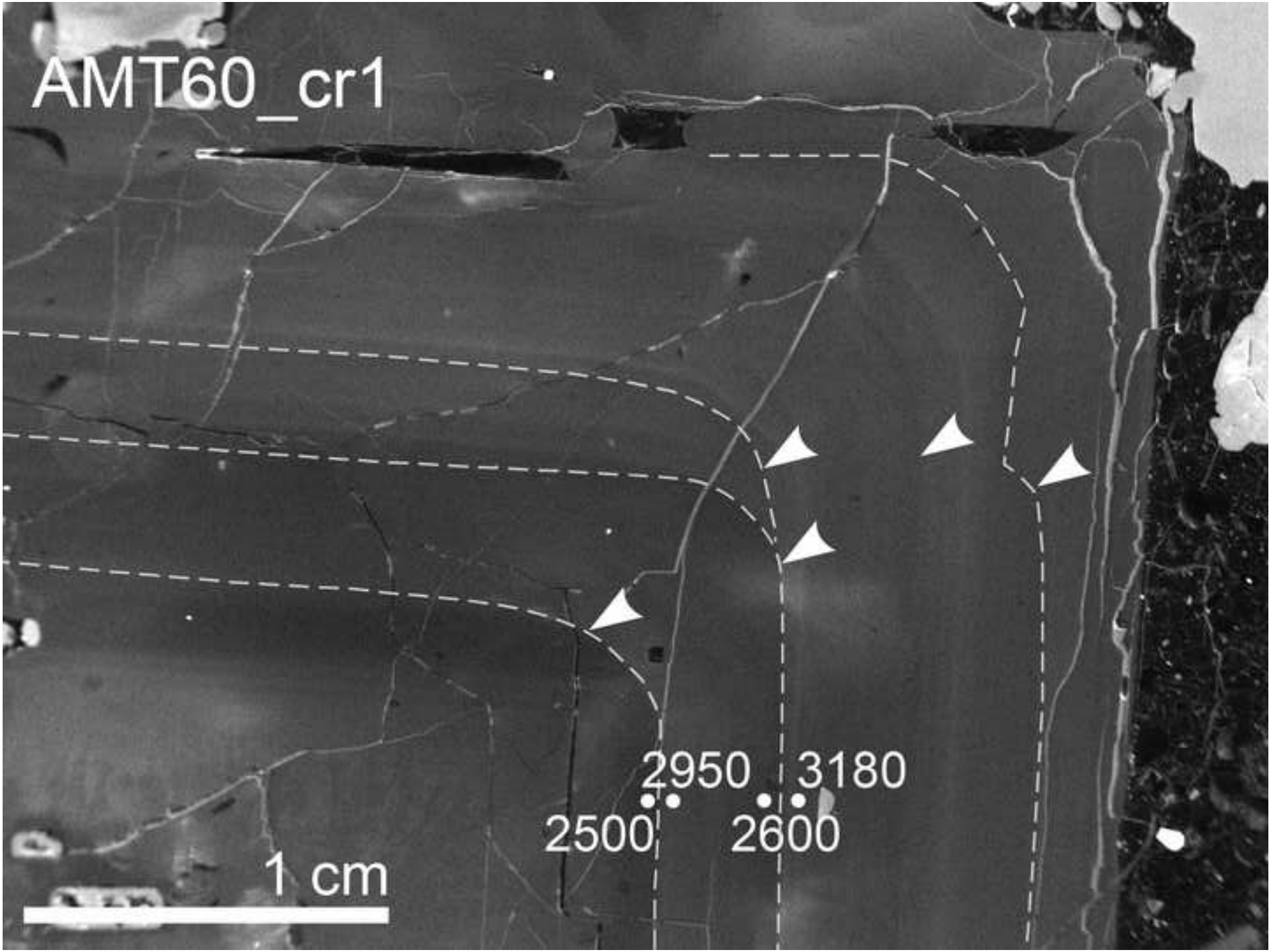

Figure7a

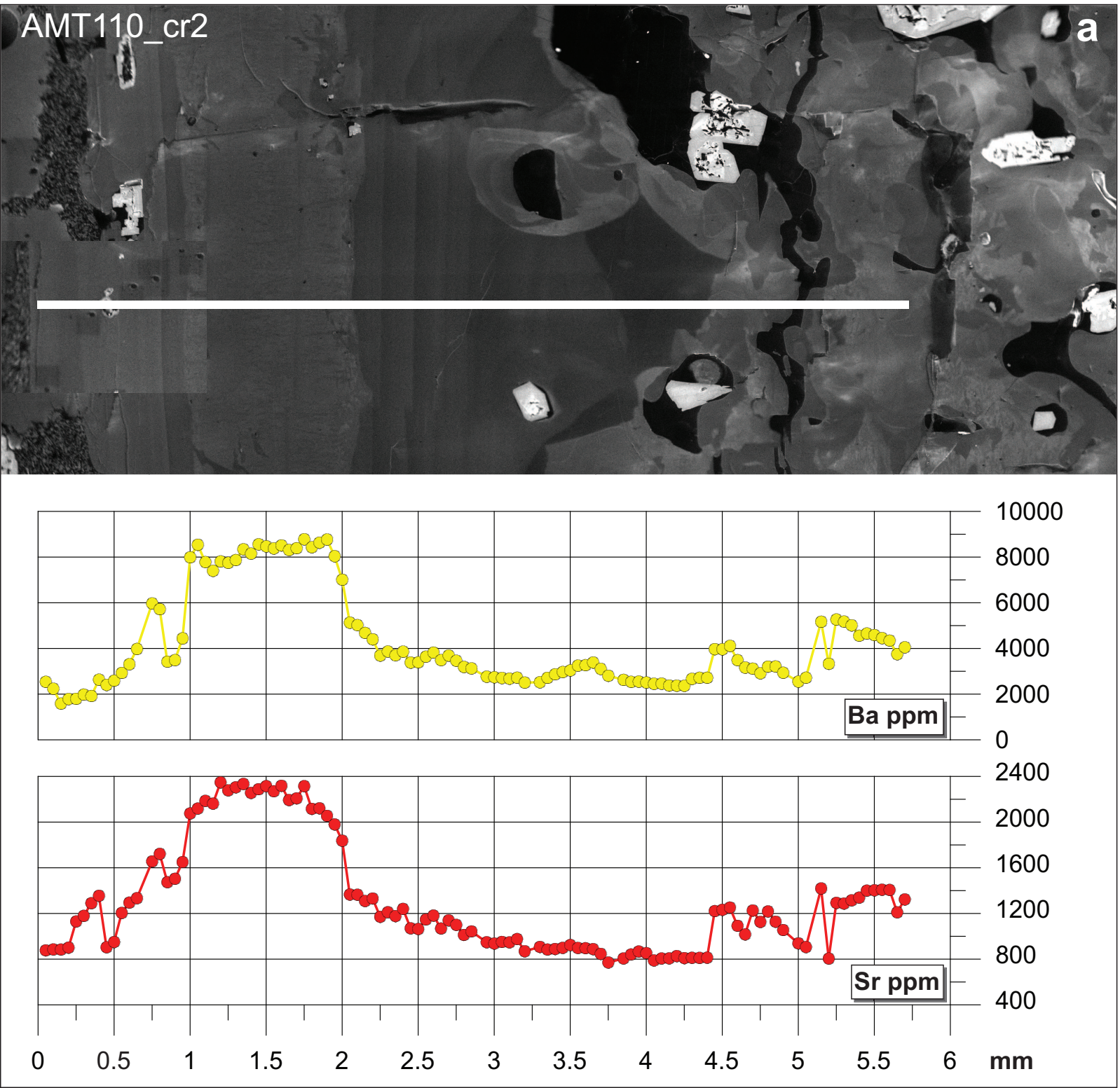
AMT110_cr2
a
Ba ppm
Sr ppm
10000
8000
6000
4000
2000
0
2400
2000
1600
1200
800
400
0
0.5
1
1.5
2
2.5
3
3.5
4
4.5
5
5.5
6
mm

Figure7b

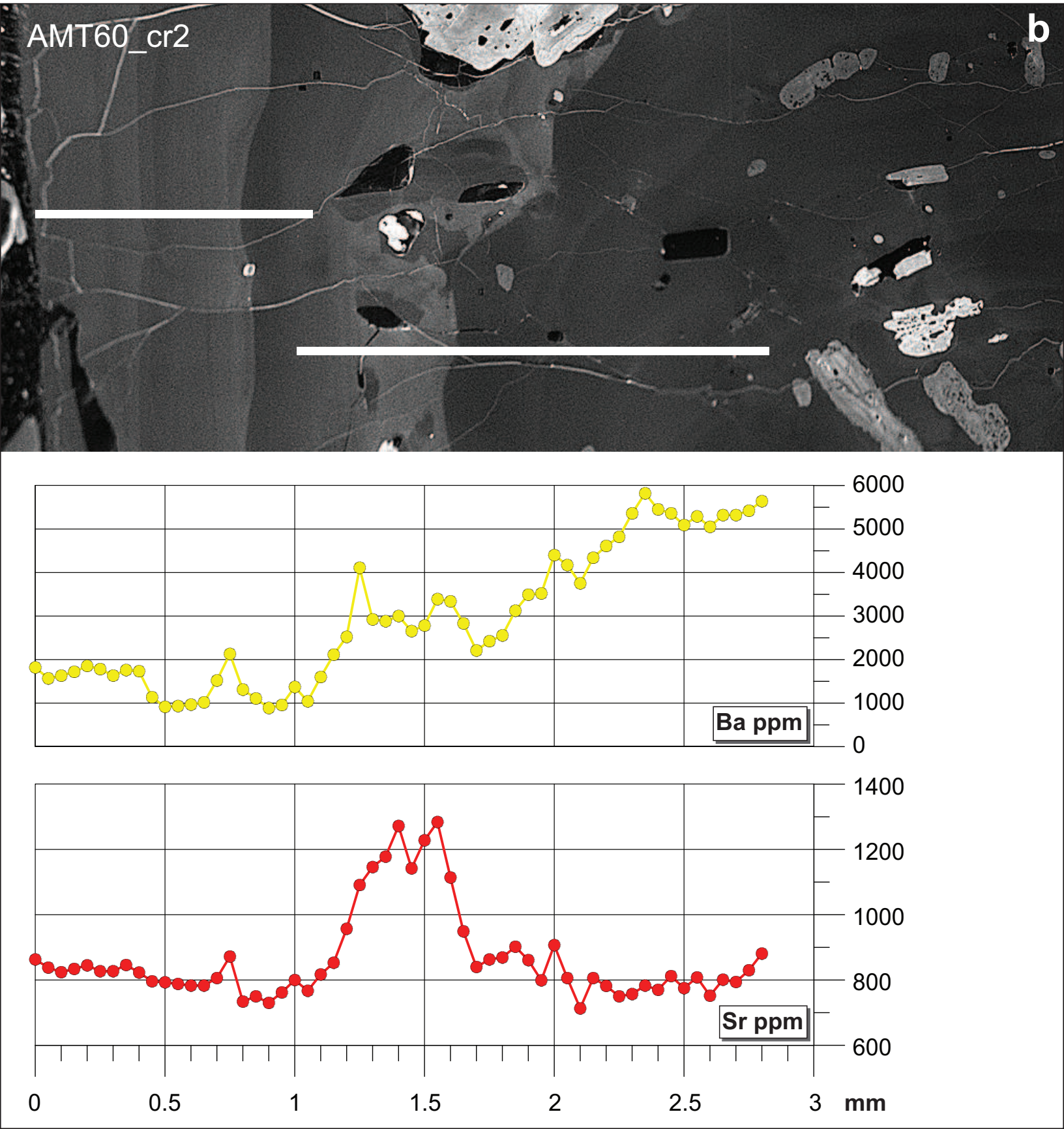
AMT60_cr2
b
6000
5000
4000
3000
2000
1000
0
Ba ppm
1400
1200
1000
800
600
Sr ppm
0
0.5
1
1.5
2
2.5
3
mm

Figure7c

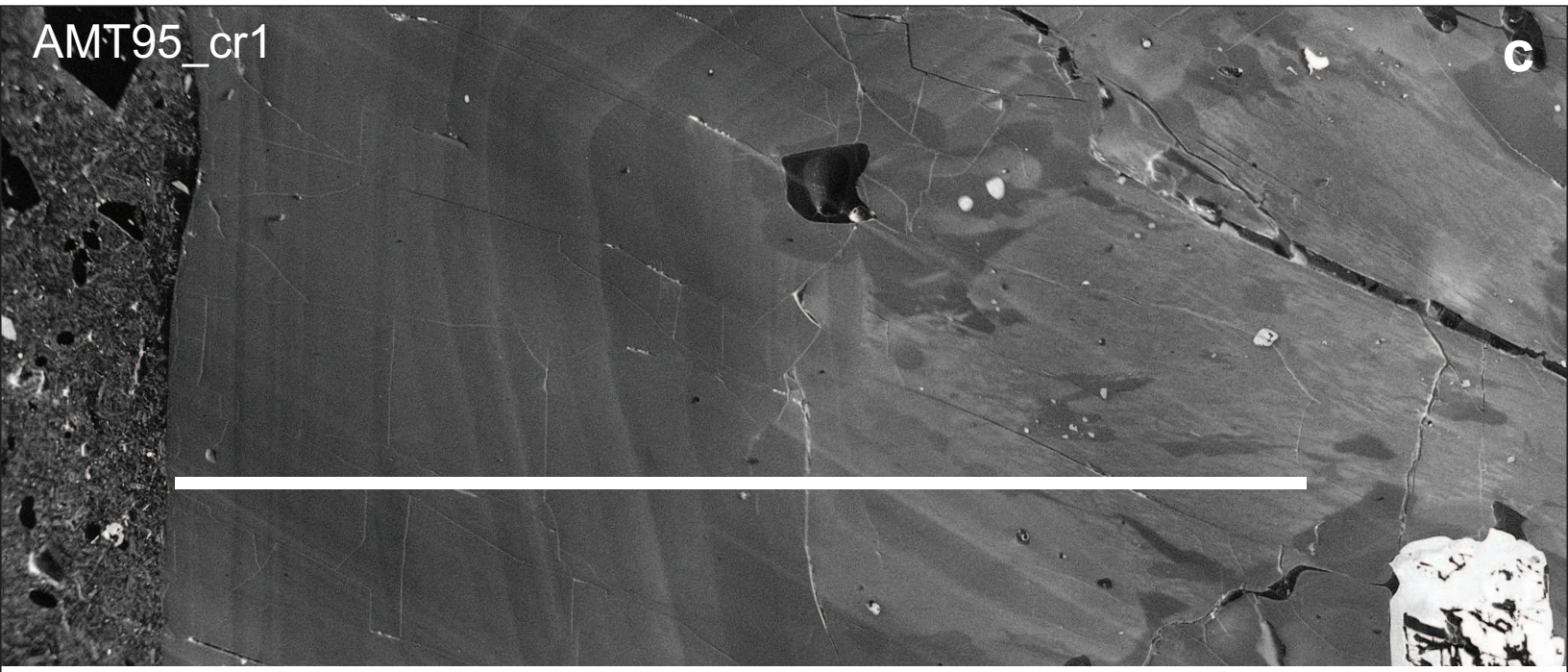
AMT95_cr1
c

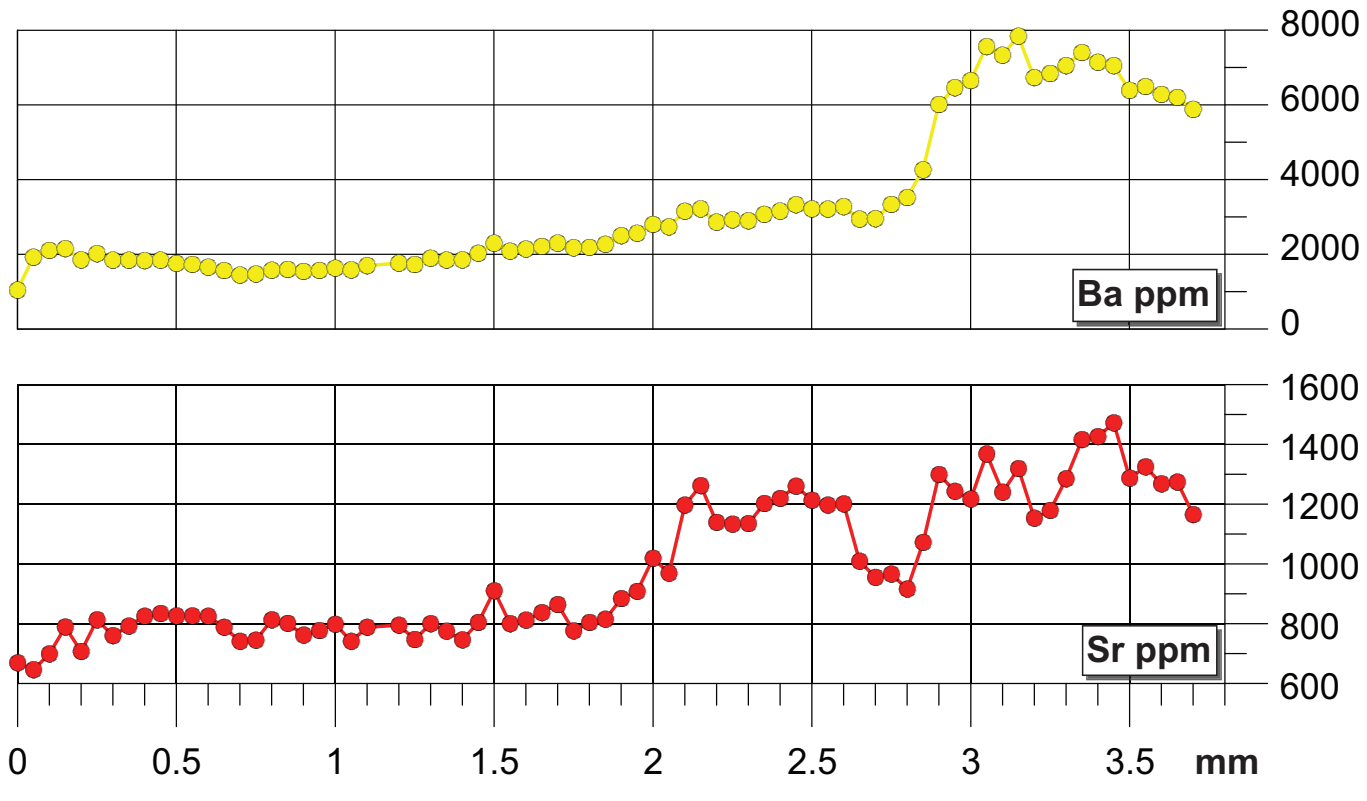
8000
6000
4000
2000
0
Ba ppm
1600
1400
1200
1000
800
600
Sr ppm
0
0.5
1
1.5
2
2.5
3
3.5
mm

Figure8

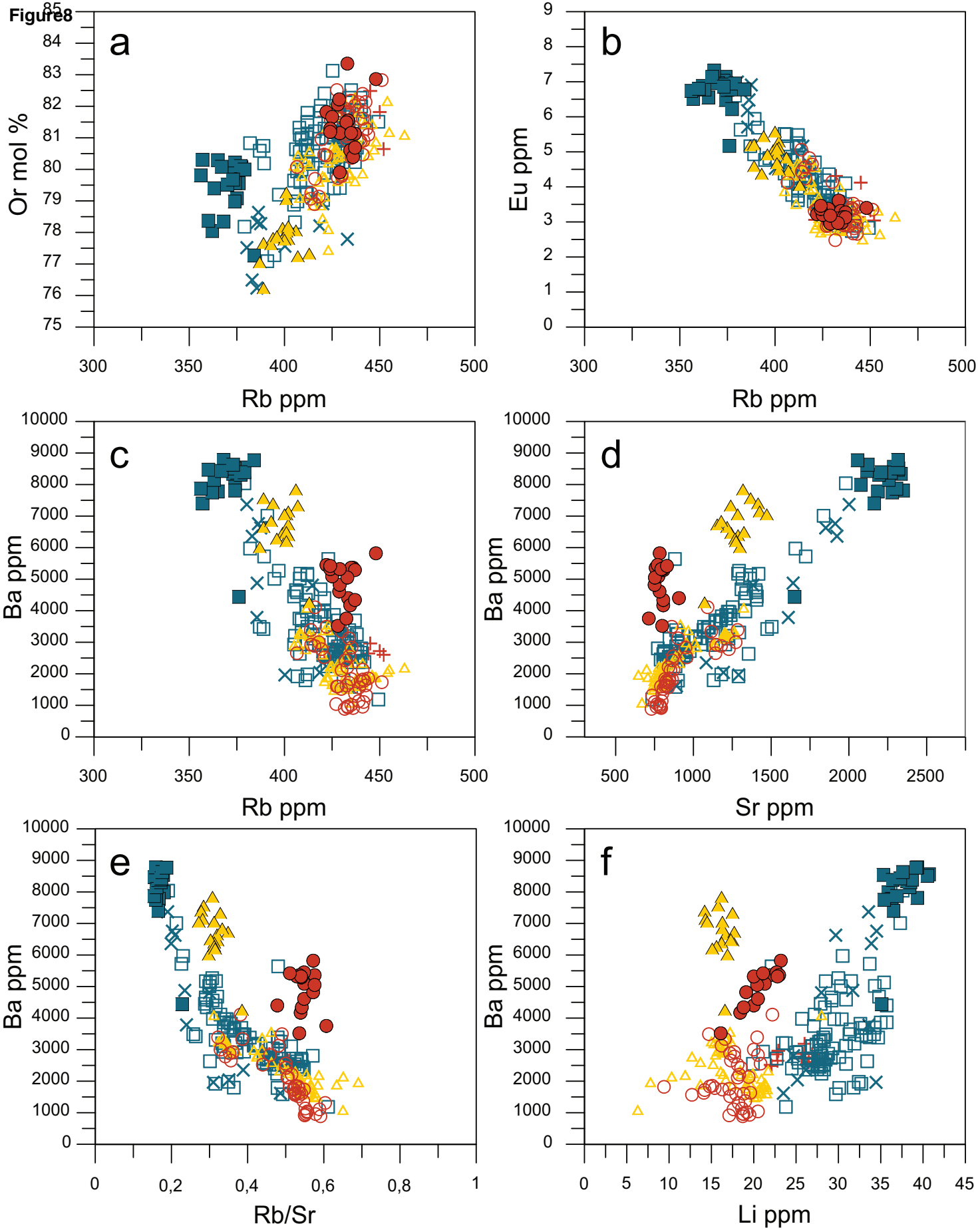

AMT60_cr2 HBa portion between 2-3 mm AMT60_cr1

AMT95_cr1 HBa portion between 2.9-3.7 mm

AMT110_cr2 HBa portion between 1-2 mm AMT110_cr1

Figure9
Click here to download high resolution image

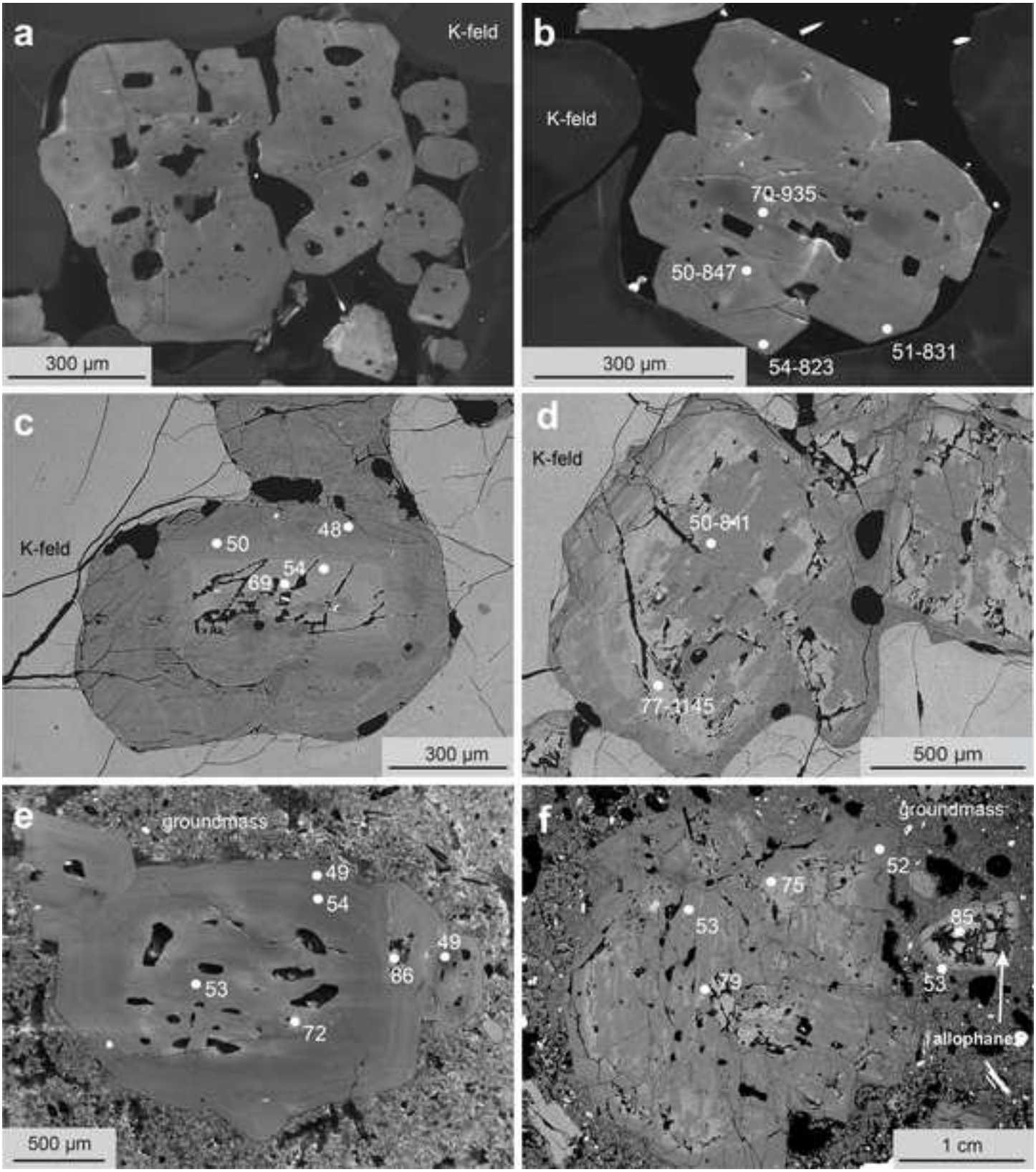

Figure 6

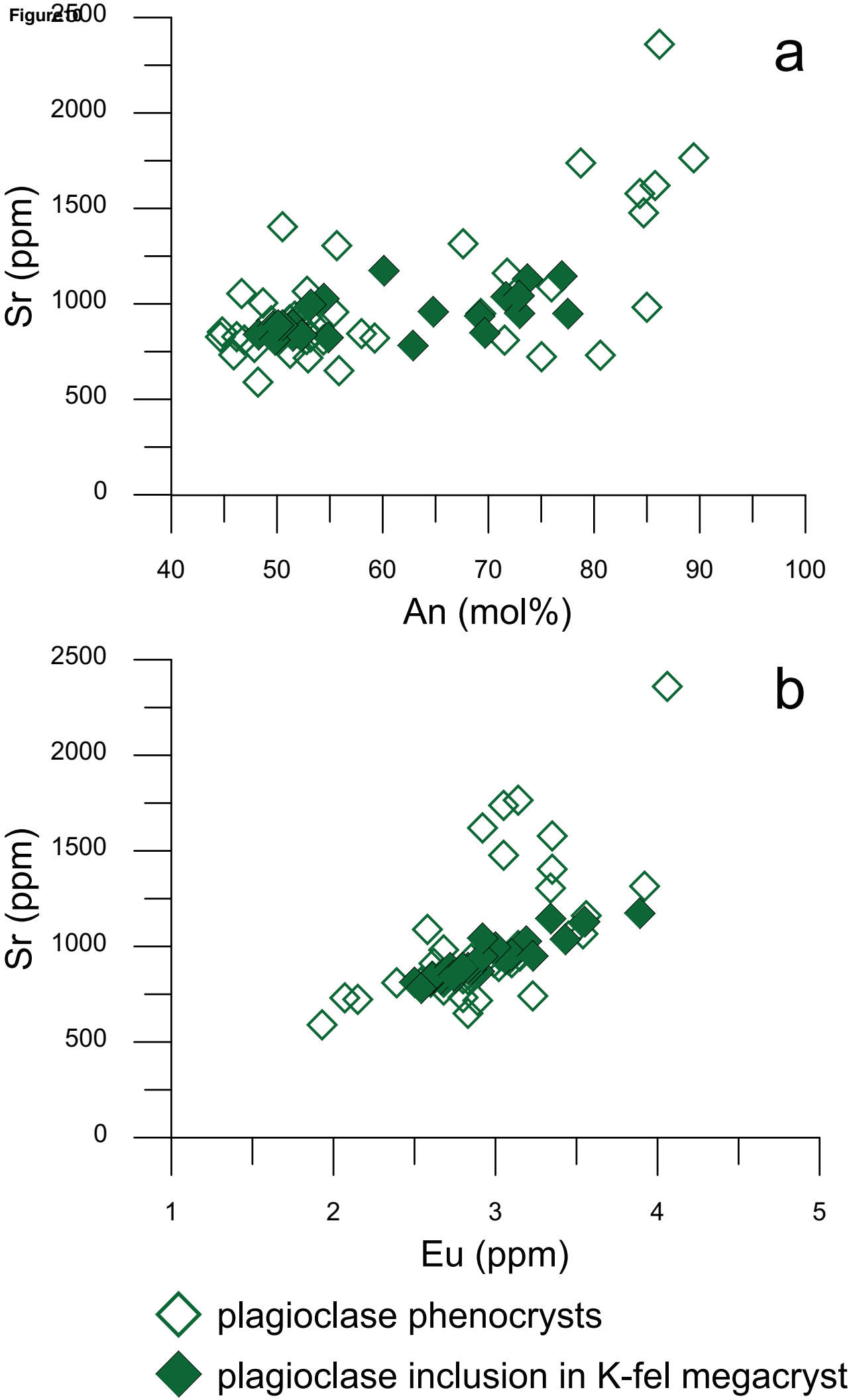
a
Sr (ppm)
2500
2000
1500
1000
500
0
40
50
60
70
80
90
100
An (mol%)
b
Sr (ppm)
2500
2000
1500
1000
500
0
1
2
3
4
5
Eu (ppm)
plagioclase phenocrysts
plagioclase inclusion in K-fel megacryst

Figure11

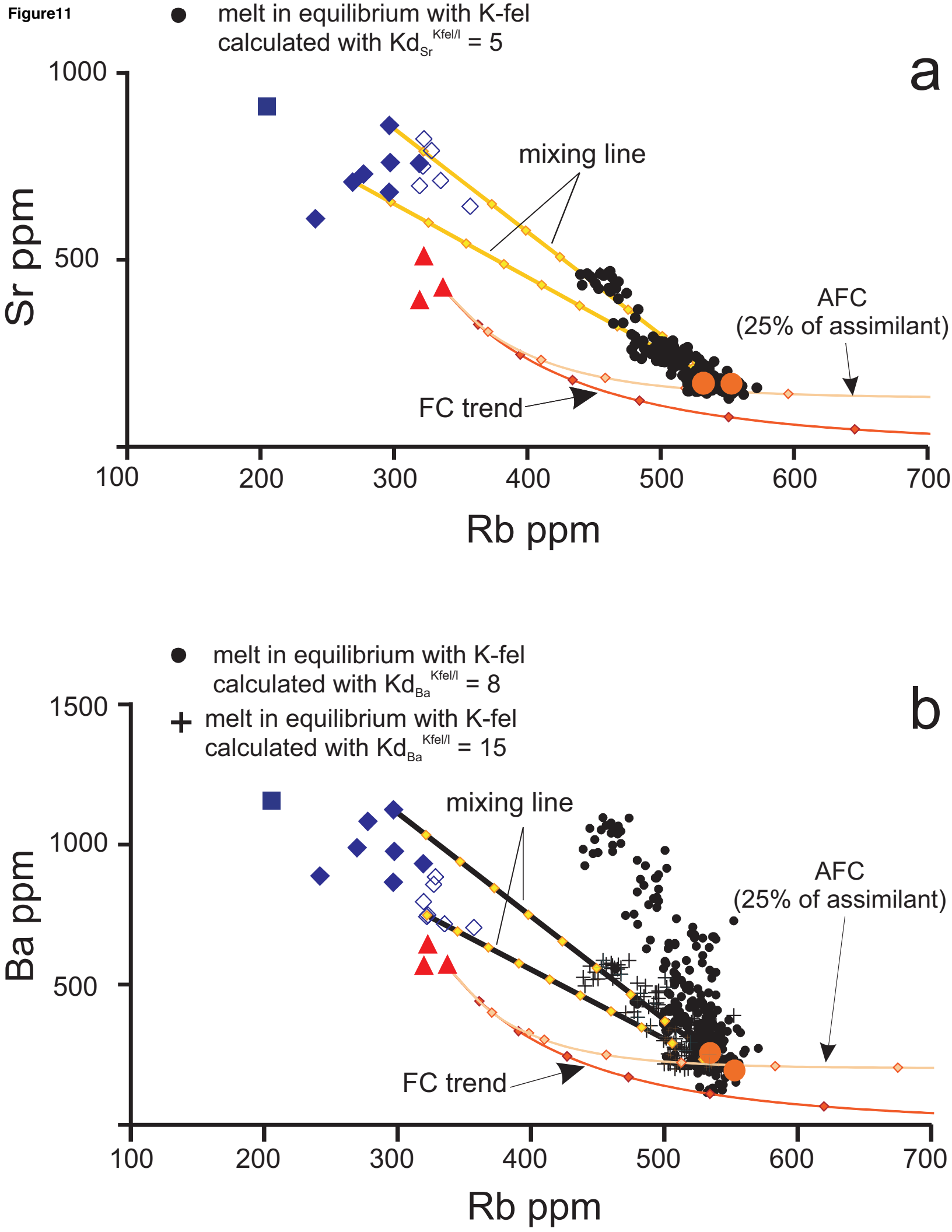
melt in equilibrium with K-fel
calculated with Kd$_{Sr}^{Kfel/l}$ = 5
a
1000
500
Sr ppm
mixing line
AFC
(25% of assimilant)
FC trend
100
200
300
400
500
600
700
Rb ppm
melt in equilibrium with K-fel
calculated with Kd$_{Ba}^{Kfel/l}$ = 8
melt in equilibrium with K-fel
calculated with Kd$_{Ba}^{Kfel/l}$ = 15
b
1500
1000
500
Ba ppm
mixing line
AFC
(25% of assimilant)
FC trend
100
200
300
400
500
600
700
Rb ppm

Figure12

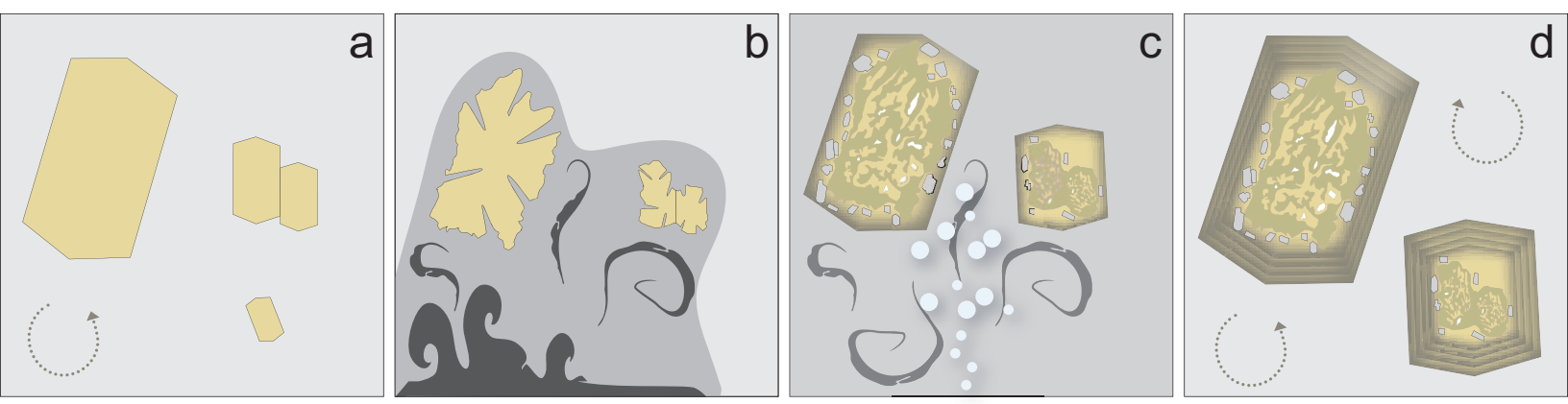

Table1
Click here to download Table: TABLE 1.docx

Table 1 – Major and trace elements composition of whole rocks from La Felice et al. (2017) and matrix glasses (this work). bdl= below detection limit.

SAMPLE	**AMT60**	**AMT95**	**AMT110**	**AMT60**		**AMT110**	
Locality	Coderino	Amiata top	Montagnola	Coderino		Montagnola	
	whole rock			*glasses average (10)*		*glasses average (6)*	
					st.dev.		*st.dev.*
SiO_2%	61.70	61.50	62.30	76.09	1.14	75.21	1.05
TiO_2	0.57	0.63	0.60	0.28	0.05	0.23	0.04
Al_2O_3	17.00	16.35	16.25	11.73	0.32	12.28	0.34
Fe_2O_3	4.36	4.84	4.23	0.84	0.21	1.23	0.08
MnO	0.07	0.08	0.07	0.02	0.03	0.03	0.03
MgO	1.93	2.58	1.74	0.05	0.05	0.10	0.03
CaO	3.27	4.50	3.45	0.68	0.36	0.87	0.10
Na_2O	2.13	2.12	2.20	2.17	0.27	2.12	0.15
K_2O	5.54	5.95	5.83	7.02	0.22	6.92	0.25
Cr_2O_3	0.01	0.01	0.01				
P_2O_5	0.19	0.23	0.19				
LOI	4.81	1.62	2.14				
Total	101.58	100.41	99.01	98.86	1.06	98.87	1.09
Ba ppm	565	642	565	193	45	255	29
Ce	151	139	144	169.8	8.0	175.2	5.8
Cr	40	50	30	bdl		bdl	
Cs	35.9	35.6	33	76.2	5.1	73.7	1.8
Dy	5.99	5.32	5.25	6.43	0.31	6.58	0.38
Er	3.08	2.67	2.65	3.27	0.18	3.22	0.12
Eu	1.46	1.73	1.6	0.61	0.12	0.62	0.07
Ga	21.5	19.5	20.4	18.79	1.45	18.03	0.68
Gd	8.07	7.74	7	8.20	0.55	8.36	0.65
Hf	8.6	7	7.5	5.76	0.22	5.63	0.32
Ho	1.19	1.03	0.99	1.22	0.06	1.23	0.11
La	83.3	76.7	79.8	90.2	3.5	91.3	2.3
Lu	0.44	0.38	0.37	0.46	0.02	0.44	0.03
Nb	17.5	15.4	18.1	15.1	0.8	15.8	0.5
Nd	68.1	63.4	62.7	65.1	3.0	68.0	2.5
Pr	18.25	16.45	16.85	18.10	0.87	18.66	0.60
Rb	319	322	337	553	31	534	12
Sm	11.6	11.05	10.95	11.28	0.54	12.11	0.62
Sn	11	9	10				
Sr	387	504	421	166	43	165	25
Ta	1.4	1.2	1.4	1.82	0.11	1.78	0.09
Tb	1.12	1.04	0.96	1.14	0.06	1.17	0.07
Th	44.3	39.4	41.8	69.1	3.3	68.4	1.9
Tm	0.5	0.44	0.43	0.48	0.03	0.48	0.04
U	12.65	11	11.2	18.5	1.1	18.5	0.5
V	55	84	59	3.0	0.5	8.7	0.9
W	7	7	7				
Y	33.1	29.2	28.8	33.9	1.5	35.4	1.7
Yb	2.64	2.45	2.46	3.11	0.25	3.01	0.12
Zr	333	260	299	165.4	6.2	170.3	10.7
As	54	27	25				
Co	8	14	8	1.13	0.35	1.88	0.53
Cu	12	23	16	2.41	2.05	1.96	0.32
Li	120	110	110	229	16	224	13
Ni	10	20	11	0.58	0.22	bdl	-
Pb	59	54	57	80.9	7.0	70.7	2.9
Sc	9	12	9	10.9	0.4	12.7	0.5
Zn	59	62	57	31.1	7.9	29.6	4.2

Table2
Click here to download Table: TABLE 2.docx

Table 2 – Modal analyses in vol% of phenocrysts in the analyzed samples. Abbreviations: plg=plagioclase; K-fel=K-feldspar; opx=orthopyroxene; cpx=clinopyroxene; bt=biotite; ox=Fe-Ti oxydes; qtz=quartz; gdm= groundmass.

Sample	AMT60	AMT95	AMT110
plg	13.2	11.6	12.8
K-fel	14.2	10.6	11.0
opx	5.2	5.0	5.3
cpx	1.3	5.1	1.7
bt	2.9	2.4	3.6
ox	0.2	0.0	0.5
qtz	0.1	0.1	0.3
gdm	63.0	65.2	64.8
Total	100	100	100